

A volume-limited sample of X-ray galaxy groups and clusters - II. X-ray cavity dynamics

E. K. Panagoulia^{1*}, A. C. Fabian¹, J. S. Sanders² and J. Hlavacek-Larrondo^{3,4}

¹*Institute of Astronomy, Madingley Road, Cambridge CB3 0HA*

²*Max-Planck-Institute für extraterrestrische Physik, 85748, Garching, Germany*

³*Kavli Institute for Particle Astrophysics and Cosmology, Stanford University, 452 Lomita Mall, Stanford, CA 94305-4085, USA*

⁴*Department of Physics, Stanford University, 452 Lomita Mall, Stanford, CA 94305-4085, USA.*

Accepted . Received ; in original form

ABSTRACT

We present the results of our study of a volume-limited sample ($z \leq 0.071$) of 101 X-ray galaxy groups and clusters, in which we explore the X-ray cavity energetics. Out of the 101 sources in our parent sample, X-ray cavities are found in 30 of them, all of which have a central cooling time of ≤ 3 Gyr. New X-ray cavities are detected in three sources. We focus on the subset of sources that have a central cooling time of ≤ 3 Gyr, whose active galactic nucleus (AGN) duty cycle is $\simeq 61$ percent (30/49). This rises to >80 percent for a central cooling time of ≤ 0.5 Gyr. When projection effects and central radio source detection rates are considered, the actual duty cycle is probably much higher. In addition, we show that data quality strongly affects the detection rates of X-ray cavities. After calculating the cooling luminosity and cavity powers of each source with cavities, it is evident that the bubbling process induced by the central AGN has to be, on average, continuous, to offset cooling. We find that the radius of the cavities, r , loosely depends on the ambient gas temperature as $r \propto T^{0.5}$, above about 1.5 keV, with much more scatter below that temperature. Finally, we show that, at a given location in a group or cluster, larger bubbles travel faster than smaller ones. This means that the bubbles seen at larger distances from cluster cores could be the result of the merging of several smaller bubbles, produced in separate AGN cycles.

Key words: galaxies: clusters: general

1 INTRODUCTION

The central cooling time in many groups and clusters of galaxies is ≤ 1 Gyr. If no heating is present, a cooling flow (Fabian 1994) would be expected to form, wherein the gas cools out of the X-ray phase, and accretes onto the central galaxy. This gas would eventually form molecular clouds, and form stars. Studies of cooling flows with *XMM-Newton* and *Chandra* have confirmed the presence of positive temperature gradients and short cooling times in the cores of clusters, which are the fingerprint of a cooling flow. However, the amount of gas observed to be cooling at temperatures 2–3 times lower than the virial temperature, is overpredicted by the cooling flow model (McNamara & Nulsen 2007, 2012; Peterson & Fabian 2006). In addition, UV and optical observations have shown that star formation rates in cluster cores are about an order of magnitude lower than predicted

(Johnstone et al. 1987; Nulsen et al. 1987), as is the amount of cold gas (e.g. Edge 2001).

Several mechanisms have been proposed over the years, which could suppress the cooling flux at lower energies, while maintaining the high cooling rates. The most prevalent solution to the cooling flow problem is that cooling is balanced, or almost so, by heating. This almost definitely requires the existence of one or more heating mechanisms, which work in a self-regulating feedback loop. Thermal conduction from the hot outer layers of clusters is one such mechanism that has been suggested. In some cases, it may be capable of balancing a cooling flow (e.g. Tucker & Rosner 1983; Voigt et al. 2002), though it can be unstable and needs fine tuning (Soker 2003). Furthermore, thermal conduction cannot offset cooling in all clusters (Voigt et al. 2002), and is not considered a general solution to the cooling flow problem. Other heating mechanisms, such as cosmic rays (Loewenstein et al. 1991) and supernovae (McNamara et al. 2004), may provide additional heating, but overall these mechanisms are unable to balance radiative losses.

* E-mail: epanagoulia@ast.cam.ac.uk

By far the most favoured heating mechanism is feedback from the central active galactic nuclei (AGNs) in clusters. Outbursts deposit large amounts of energy into the surrounding ICM, which are sufficient to reduce, or even quench, cooling flows (for reviews, see McNamara & Nulsen 2007, 2012; Fabian 2012; Gitti et al. 2012). Many studies now support the fact that AGN affect their surrounding intracluster medium (ICM) (e.g. Birzan et al. 2004; Dunn & Fabian 2008), though the details of this process are still poorly defined. The detection of X-ray cavities in *Chandra* images of many clusters gave credence to the idea that it is indeed AGN feedback that primarily heats up the ICM. These images show radio lobes displacing the ICM, leaving behind X-ray surface brightness (SB) depressions. These depressions are cospatial with radio emission seen from the radio lobes, as seen in e.g. Perseus (Fabian et al. 2000; Böhringer et al. 1993) and Hydra A (McNamara et al. 2000; Nulsen et al. 2002). The displacement of the hot ICM gas creates a low-density, buoyantly rising bubble in the ICM, which is in pressure equilibrium with its surrounding gas. Observations also show X-ray SB depressions coincident with radio emission of a very low frequency. These have been dubbed “ghost cavities”, and are believed to originate from past AGN outbursts, and whose high-frequency radio emission has since faded (e.g. the ghost cavities in Abell 2597 and the Hydra A cluster, McNamara et al. 2001; Wise et al. 2007, respectively).

X-ray cavities provide a reliable method of obtaining lower limits on the energy output of AGN outbursts, through measuring the enthalpy of the X-ray cavities, under the assumption that they are in pressure equilibrium with the surrounding gas. In addition, it is possible to measure the power associated with AGN feedback processes, by calculating either the time it would take the bubble to buoyantly rise to its present position, or the time required to inflate the bubble at the local sound speed (e.g. Birzan et al. 2004). The latter assumes that there are no strong shocks driven into the ICM by the bubbles, and so the bubbles are being inflated at a speed similar to the local sound speed.

X-ray cavities also provide a unique insight into how the AGN feedback cycle works. 60–70 per cent of cool core (CC) clusters have radio sources (Burns 1990; Mittal et al. 2009; Birzan et al. 2012), and, of the clusters that require heating (i.e. are likely to be CC clusters), a similar fraction display bubbles (Dunn et al. 2005; Dunn & Fabian 2006). Furthermore, the process of creating bubbles in cluster cores is thought to be the main method of transferring energy from the AGN to the cluster core, and so preventing the occurrence of runaway cooling. This in turn generates pressure (i.e. sound) waves in the ICM, which can carry energy out to large distances from the cluster centre, in the form of continuous heating, which is distributed as is necessary (Fabian et al. 2003; Voigt & Fabian 2004).

Several extensive studies on X-ray cavity dynamics have been done before, by a number of authors (e.g. Dunn & Fabian 2006; Rafferty et al. 2006; Birzan et al. 2012; Hlavacek-Larrondo et al. 2012). However, these studies have primarily focused on the brightest sources in the sky, or on a particular type of sources. For example, Birzan et al. (2012) study the Brightest 55 clusters of galaxies (B55) and the Highest X-ray FLUX Galaxy Cluster Sample (HIFLUGCS), Dunn & Fabian (2006) analyse a subsample of the B55 sam-

ple, while Rafferty et al. (2006) examine a sample of 33 galaxies that are located at the centre of a cooling flow. This means that quite a lot of past studies are flux-limited, and focus predominantly on galaxy clusters.

In this paper, we examine a distance- and X-ray luminosity-limited parent sample of 101 clusters and groups. We use unsharp-masking to examine whether individual sources in our parent sample harbour X-ray cavities. We then focus on a subsample of 49 clusters and groups, all of which have central cooling times ≤ 3 Gyr, and study their X-ray cavity “demographics”. The larger parent sample is discussed in detail in Panagoulia et al. (2014) (hereafter referred to as Paper I). The parent sample and subsample selection are discussed in Section 2. The data preparation is briefly summarised in Section 3. The extraction of cooling time profiles is described in Section 4, and the imaging analysis is outlined in Section 5. The results of our analysis are presented and discussed in Section 6.

In this paper, we adopt a flat Λ CDM cosmology, with $H_0 = 71 \text{ km s}^{-1} \text{ Mpc}^{-1}$, $\Omega_m = 0.27$ and $\Omega_\Lambda = 0.73$. All abundances in this paper are relative to solar, as defined in Anders & Grevesse (1989). In all the images shown in this paper, north is to the top and east is to the left. The error-bars presented are at 90 percent confidence, unless otherwise stated.

2 A VOLUME-LIMITED SAMPLE OF GROUPS AND CLUSTERS OF GALAXIES

The motivation behind the work in both this paper and Paper I, is the study of the radial properties of the ICM in X-ray groups and clusters of galaxies. Ultimately, we aim to determine the importance and the effect of non-gravitational processes, such as AGN feedback, on the ICM. We are specifically interested in cluster cores (the central ~ 10 kpc), for which we need high spatial resolution data. For this reason, we chose to look at a sample of nearby groups and clusters of galaxies, for which *Chandra* and/or *XMM-Newton* data are available.

For details on the sample selection, we refer readers to Section 2 of Paper I. We briefly summarise the selection process below:

- Using the Northern *ROSAT* All Sky catalogue (NORAS; Böhringer et al. 2000) and the *ROSAT-ESO* Flux Limited X-ray galaxy cluster survey (REFLEX; Böhringer et al. 2004), we constructed a volume-limited sample of sources. These were chosen to lie at a distance of ≤ 300 Mpc. In total, 289 sources from these catalogues meet this criterion.

- We require a statistically complete sample, so we make cuts in the X-ray luminosity, L_X , as well as distance, to avoid groups of sources that have no data. For details of the cuts in distance and L_X , see section 2 of Paper I.

- After the cuts in both L_X and distance, we end up with a final sample, containing 101 sources. Of these 101 sources, all but four of them have *Chandra* and/or *XMM-Newton* data. Where possible, we use *Chandra* data, to benefit from the higher spatial resolution and lower background levels of the Advanced CCD Imaging Spectrometer (ACIS) detectors. The details of all the sources in our sample, and the observations used in subsequent data analysis, are given in Tables 1–4 in Paper I.

Source name	Alt. source name	RA (2000)	DEC (2000)	Redshift	L_X ($\times 10^{44}$ erg s $^{-1}$)	Radio	Central t_{cool} (Gyr)
(1)	(2)	(3)	(4)	(5)	(6)	(7)	(8)
RXCJ1242.8+0241	NGC 4636	190.7063	2.6856	0.0031	0.01	yes (1)	$0.19^{+0.17}_{-0.04}$
RXCJ1229.7+0759	M 49-Virgo-NGC 4472	187.4403	7.9870	0.0033	0.01	yes (2)	$0.04^{+0.002}_{-0.003}$
RXCJ0338.4-3526	FORNAX-NGC 1399	54.6167	-35.4483	0.0051	0.012	yes (1)	$0.06^{+0.004}_{-0.003}$
RXCJ1501.2+0141	NGC 5813	225.3016	1.6960	0.0065	0.02	yes (3)	0.18 ± 0.01
RXCJ1506.4+0136	NGC 5846	226.6250	1.6022	0.0066	0.008	yes (2)	$0.15^{+0.02}_{-0.01}$
RXCJ1315.3-1623	NGC 5044	198.8500	-16.3897	0.0087	0.097	yes (2)	$0.22^{+0.03}_{-0.02}$
RXCJ1248.7-4118	A 3526-NGC 4696	192.20	-41.3078	0.0114	0.721	yes (1, 2)	$0.09^{+0.004}_{-0.003}$
RXCJ1036.6-2731*	A 1060	159.1750	-27.5244	0.0126	0.297	yes (1)	0.32 ± 0.04
RXCJ0419.6+0224	NGC 1550	64.9083	2.4139	0.0131	0.153	yes (1)	$0.19^{+0.02}_{-0.03}$
RXCJ1751.7+2304*	NGC 6482	267.9480	23.0705	0.0132	0.02	yes (13)	$0.15^{+0.035}_{-0.006}$
RXCJ1253.0-0912	HCG 62	193.2750	-9.2003	0.0146	0.037	yes (4)	$0.19^{+0.02}_{-0.01}$
RXCJ1050.4-1250	NGC 3402	162.6083	-12.8464	0.0155	0.059	yes (14)	$0.098^{+0.014}_{-0.003}$
RXCJ0152.7+3609	A 0262	28.1948	36.1513	0.0163	0.81	yes (1)	0.13 ± 0.02
RXCJ0200.2+3126	NGC 0777	30.0687	31.4365	0.0168	0.04	yes (5)	$0.325^{+0.024}_{-0.004}$
RXCJ0125.5+0145*	NGC 533	21.3750	1.7622	0.0174	0.032	yes (2)	$0.10^{+0.02}_{-0.01}$
RXCJ1204.4+0154*	MKW 4	181.1065	1.9010	0.0195	0.28	yes (1)	$0.24^{+0.07}_{-0.02}$
RXCJ1407.4-2700	A 3581	211.8667	-27.0153	0.0230	0.316	yes (6)	$0.29^{+0.02}_{-0.04}$
RXCJ1223.1+1037	NGC 4325	185.7772	10.6240	0.0258	0.20	yes (15)	$0.27^{+0.06}_{-0.03}$
RXCJ1715.3+5724	NGC 6338	258.8414	57.4074	0.0276	0.49	yes (7)	$0.22^{+0.05}_{-0.02}$
RXCJ1628.6+3932	A 2199	247.1582	39.5487	0.0299	3.77	yes (1)	$0.48^{+0.06}_{-0.09}$
RXCJ0433.6-1315	A 0496	68.4083	-13.2592	0.0326	1.746	yes (1)	$0.33^{+0.04}_{-0.09}$
RXCJ0338.6+0958	2A0335+096	54.6699	9.9745	0.0347	4.21	yes (1)	0.16 ± 0.02
RXCJ1516.7+0701	A 2052	229.1834	7.0185	0.0353	2.58	yes (1)	$0.21^{+0.06}_{-0.11}$
RXCJ0425.8-0833*	RBS 0540	66.4625	-8.5592	0.0397	1.008	yes (1)	$0.33^{+0.14}_{-0.05}$
RXCJ1521.8+0742	MKW3s	230.4582	7.7088	0.0442	2.70	yes (1)	0.09 ± 0.03
RXCJ1252.5-3116*	-	193.1417	-31.2678	0.0535	0.861	yes (16)	$0.32^{+0.12}_{-0.04}$
RXCJ0041.8-0918	A 85	10.4583	-9.2019	0.0555	5.293	yes (1)	$0.40^{+0.11}_{-0.03}$
RXCJ2313.9-4244	A S1101	348.4958	-42.7339	0.0564	1.738	yes (1)	$0.34^{+0.08}_{-0.05}$
RXCJ0102.7-2152	A 0133	15.6750	-21.8736	0.0569	1.439	yes (1)	0.18 ± 0.03
RXCJ2205.6-0535*	A 2415	331.4417	-5.5933	0.0582	1.135	yes (8)	$0.48^{+0.13}_{-0.04}$
RXCJ1454.5+1838	A 1991	223.6309	18.6420	0.0586	1.46	yes (8)	0.23 ± 0.01
RXCJ1348.8+2635	A 1795	207.2207	26.5956	0.0622	9.93	yes (1, 8)	$0.27^{+0.12}_{-0.06}$
RXCJ0123.1+3327	NGC 499	20.7970	33.4620	0.0153	0.04	no (2)	$0.68^{+0.12}_{-0.03}$
RXCJ1627.3+4240*	A 2192	246.8482	42.6784	0.0317	0.12	yes (18)	$0.65^{+0.45}_{-0.01}$
RXCJ1604.9+2355*	AWM4	241.2377	23.9206	0.0326	0.55	yes (9)	$0.70^{+0.16}_{-0.06}$
RXCJ2357.0-3445	A 4059	359.2583	-34.7606	0.0475	1.698	yes (10)	$0.65^{+0.05}_{-0.06}$
RXCJ0918.1-1205	A 780 - Hydra A	139.5292	-12.0933	0.0539	2.659	yes (1)	$0.53^{+0.06}_{-0.10}$
RXCJ2336.5+2108*	A 2626	354.1262	21.1424	0.0565	1.55	yes (8)	$0.60^{+0.44}_{-0.27}$
RXCJ1303.7+1916*	A 1668	195.9398	19.2715	0.0643	1.79	yes (8)	$0.80^{+0.14}_{-0.10}$
RXCJ2347.7-2808*	A 4038	356.9292	-28.1414	0.0300	1.014	yes (1)	$1.07^{+0.45}_{-0.47}$
RXCJ1347.4-3250*	A3571	206.8667	-32.8497	0.0391	3.996	yes (1)	$1.07^{+3.01}_{-0.37}$
RXCJ2009.9-4823*	S 0851-NGC 6868	302.4750	-48.3931	0.0097	0.007	yes (2)	$1.65^{+0.34}_{-0.14}$
RXCJ1840.6-7709*	-	280.1542	-77.1556	0.0194	0.087	yes (17)	$1.59^{+0.18}_{-0.21}$
RXCJ1523.0+0836*	A2063	230.7724	8.6025	0.0355	1.94	yes (1)	$1.88^{+2.13}_{-0.77}$
RXCJ0721.3+5547*	A0576	110.3426	55.7864	0.0381	1.41	yes (1)	$1.51^{+3.40}_{-0.57}$
RXCJ1257.1-1724	A1644	194.2917	-17.4003	0.0473	1.952	yes (1)	$1.58^{+0.21}_{-0.20}$

Table 1. List of the 49 sources in our subsample and their properties.

We note that the Perseus cluster, and the central galaxies of the Virgo cluster, M86 and M87, are not included in the NORAS and REFLEX catalogues. The reason given for the exclusion of M86 and M87 is the uncertainty in making individual flux measurements for these sources, given that they are surrounded by diffuse emission from the Virgo cluster. The Perseus cluster (NGC 1275) is excluded as it

lies within the band of the Milky Way, which is defined as the region of the sky with galactic latitude $|b_{\text{II}}| \leq 20^\circ$ in both surveys (the Perseus cluster has a galactic latitude of -13.26°). This Milky Way band was excluded from both the NORAS and REFLEX surveys.

There is some overlap between our sample and those of Reiprich & Böhringer (2002) and Edge et al. (1990). We

Table 1 – *continued*

Source name (1)	Alt. source name (2)	RA (2000) (3)	DEC (2000) (4)	Redshift (5)	L_X ($\times 10^{44}$ erg s $^{-1}$) (6)	Radio (7)	Central t_{cool} (Gyr) (8)
RXCJ1733.0+4345	IC 1262	263.2607	43.7629	0.0307	0.47	yes (11)	$2.10^{+0.44}_{-0.28}$
<u>RXCJ2315.7-0222*</u>	-	348.9375	-2.3769	0.0267	0.134	yes (16)	$2.76^{+0.25}_{-0.23}$
RXCJ1254.6-2913*	A3528S	193.6708	-29.2233	0.0544	1.064	yes (12)	$2.68^{+0.81}_{-0.56}$

List of the 49 sources in our short central cooling time subsample and their properties, adapted from Paper I. (1) source name as in the REFLEX or NORAS catalogue, (2) alternative source name (sometimes referring to the central dominant galaxy), (3) and (4) source right ascension and declination in epoch 2000 coordinates, (5) source redshift, (6) source X-ray luminosity in the rest frame 0.1–2.4 keV band, (7) existence or absence of a central radio source, and (8) central cooling time in Gyr. The starred sources show no sign of X-ray cavities, and the underlined sources are the ones for which *XMM-Newton* data were used. The sources are split into 0.5 Gyr central cooling time bins (i.e. the top group have a central cooling time ≤ 0.5 Gyr, the second group 0.5–1.0 Gyr and so on). REFERENCES: (1) Birzan et al. (2012) and references therein, (2) Dunn et al. (2010), (3) Randall et al. (2011), (4) Gitti et al. (2010), (5) Ho & Ulvestad (2001), (6) Canning et al. (2013), (7) Pandge et al. (2012), (8) Owen & Ledlow (1997), (9) O’Sullivan et al. (2010), (10) Choi et al. (2004), (11) Trinchieri et al. (2007), (12) Venturi et al. (2001), (13) Goudfrooij et al. (1994), (14) O’Sullivan et al. (2007), (15) Dong et al. (2010), (16) Magliocchetti & Brüggén (2007), (17) Sydney University Molonglo Sky Survey image (SUMSS; Mauch et al. 2003), (18) NRAO VLA Sky Survey image (NVSS; Condon et al. 1998).

cross-checked the sources in these two samples with those in our sample, and find that the sources that appear in the Reiprich & Böhringer (2002) and Edge et al. (1990) samples but not ours, are either too distant, or were not included in the NORAS and REFLEX catalogues, or did not meet our sample selection criteria.

2.1 Short central t_{cool} subsample

For this work, we are particularly interested in investigating the connection between central cooling times, and the presence, or absence, of X-ray cavities. Here, we define the central cooling time as the cooling time calculated for the gas in the innermost spectral bin for each source (for details of the creation of the spectral extraction regions, see Section 4.1), which we were able to reliably calculate for 65 out of the 101 sources in our parent sample, using Equation 3 (see Section 4.2) (these are the starred sources in tables 1 and 3 in Paper I). In order to carry out a detailed analysis of the central regions of groups and clusters, a large number of counts is required there. To select the sources with the highest number of counts in their central region, we calculated the total number of counts within the central 20 kpc for all 65 groups and clusters for which we had a central cooling time. We plot the central cooling time of each source vs. the total counts in the central 20 kpc in the left-hand panel of Fig. 1. The black circles represent sources for which *Chandra* data were used in the analysis, and the black squares indicate sources for which *XMM-Newton* data were used. The filled and empty circles illustrate sources with a central cooling time of ≤ 3 Gyr and ≥ 3 Gyr, respectively. The two rightmost empty circles are Abell 3667 and the Coma cluster, both of which are well-studied major mergers. The dashed line represents the 3 Gyr cut-off in the central cooling time, in both figures. As can be seen, a cut-off of the central cooling time at ≤ 3 Gyr excludes most sources that do not have a large number of counts in their central 20 kpc. Our ≤ 3 Gyr cut-off is also in line with previous studies of relatively nearby groups and clusters of galaxies (e.g. Dunn & Fabian 2006; Dunn et al. 2010). In total, 49 sources out of the 65, that have a reliable central cooling time value, meet this requirement.

Of these sources, 15 are groups, while the rest are clusters, where we define a source as a group or cluster based on the currently available literature. As we used different, and sometimes multiple, literary sources to define a source as a group or cluster, this classification will be based on different classification criteria, such as optical richness and X-ray luminosity. Despite this variety of classification methods used for each source, the separate classifications in the literature of a source as a group or cluster are in agreement for the vast majority of the sources in our subsample. We consider all 49 sources with a central cooling time ≤ 3 Gyr to be cool cores. The 16 sources that were not included in our subsample are: IIIZW54, Abell 1736, Abell 2665, Abell 2734, Abell 3158, Abell 3376, Abell 3391, Abell 3395, Abell 3562, Abell 3667, Abell 376, Abell 754, the Coma cluster, MKW 8, NGC 6099, and RXCJ1109.7+2145. Hereafter, we refer to these 16 sources as the excluded sources. We note that many of these sources are well-studied merging clusters.

To test the validity of our selection method, we also plot the central cooling time of the 65 sources, for which we have a central cooling time measurement, against the respective count rate within the central 20 kpc. The plot is shown in the right-hand panel of Fig. 1, where the symbols are the same as in the left-hand panel of the same figure, and the rightmost empty circle is the Coma cluster. The separation between the sources with a cooling time of less than and more than 3 Gyr is now even more pronounced. In addition, we plotted the central cooling time of each of the 65 sources against the count rate within the central 20 kpc, multiplied by $(1+z)^2$, where z is the redshift of a source, to get rid of any dependence of the count rate on the redshift of the source. The result is very similar to that in the left-hand panel of Fig. 1, but with a slightly wider separation between the sources that have a central cooling time of ≥ 3 Gyr, and those with a central cooling time ≤ 3 Gyr. This indicates that there is a separation between the groups and clusters that have a central cooling time larger or smaller than 3 Gyr, that is intrinsic rather than affected by data quality.

Note that we have selected to plot the cooling time in the innermost central bin vs. the total counts or count rate

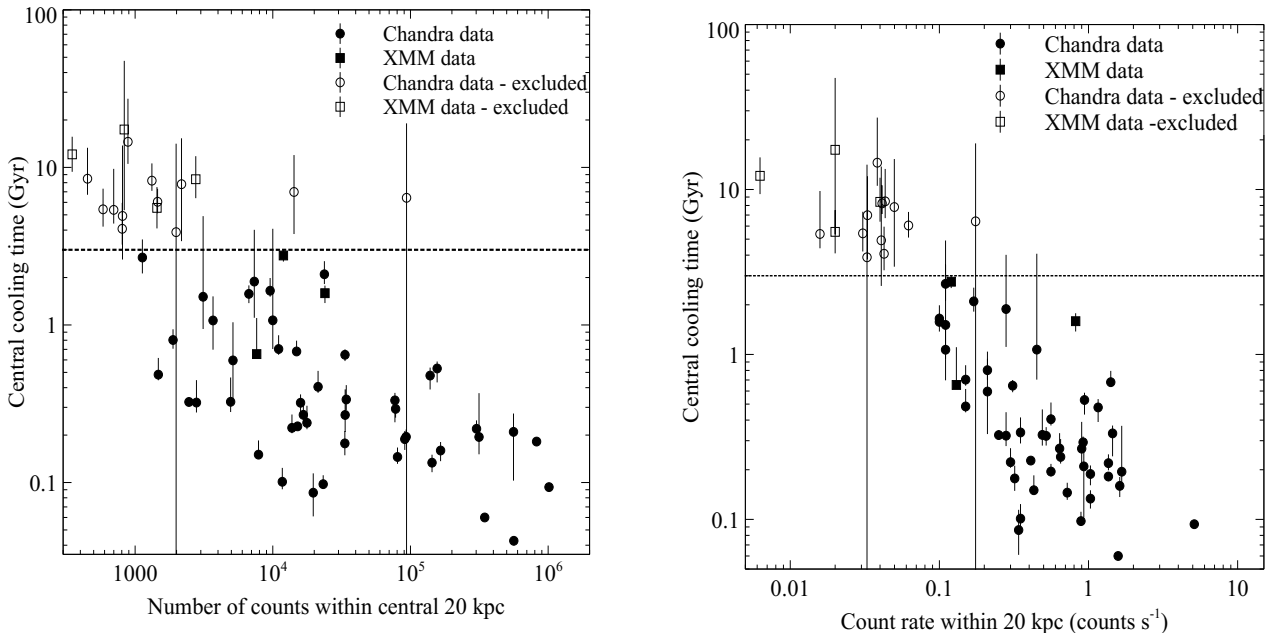


Figure 1. *Left:* Central cooling time vs. counts within the central 20 kpc for the 65 sources for which we have a central cooling time measurement. *Right:* Central cooling time vs. count rate within the central 20 kpc for the 65 sources for which we have a central cooling time measurement. In both plots, the circles and squares represent sources for which *Chandra* and *XMM-Newton* data were used in the analysis, respectively. The filled symbols indicate the sources with a central cooling time ≤ 3 Gyr, which formed our short central cooling time subsample, and the empty symbols the sources that have longer central cooling times. The rightmost empty circle in both plots is the Coma cluster. The dashed line in both plots simply represents the 3 Gyr cut-off in the central cooling time.

within the central 20 kpc of each source, as we are mainly interested in studying the cavity dynamics of this short central cooling time subsample. In sources within the redshift range we are studying, X-ray cavities are expected to lie within this radius, and not just in the region covered by the central spectral bin.

The properties of the sources in our short central cooling time subsample, as listed in the NORAS or REFLEX catalogues, and their calculated central cooling times, are given in columns 1–6 and 8 in Table 1, respectively. The sources are split into 0.5 Gyr central cooling time bins, i.e. the top group sources have a central cooling time ≤ 0.5 Gyr, the second group 0.5–1.0 Gyr, and so on. The underlined sources are the ones for whose analysis *XMM-Newton* data were used. The starred sources are the ones which show no evidence of X-ray cavities.

3 OBSERVATIONS AND DATA ANALYSIS

3.1 *Chandra* data

The observation IDs, as well as the clean exposure times, for each source are given in Tables 2 and 4 in Paper I. We refer the reader to Section 3.1 of Paper I for details of the data analysis. To summarise, new Level 2 events files were created from the Level 1 event files, using the CIAO ACIS_REPROCESS_EVENTS pipeline. Background lightcurves were generated and examined, in order to excise periods of X-ray background flaring. Blank-sky observations were selected and adjusted to match individual observations, and were used to create background images and spectra. If more

than one dataset was available for each source, the datasets were reprojected onto the same set of coordinates. Finally, a 0.5–7.0 keV background-subtracted and exposure-corrected image was made for each source, and examined to identify contaminating point sources. These were then excluded from subsequent spectral analysis.

3.2 *XMM-Newton* data

For details of the analysis of the *XMM-Newton* data, see Section 3.2 in Paper I. We used data from all three EPIC detectors, and these were reprocessed using EMCHAIN and EPCHAIN for the MOS and pn, respectively. Lightcurves were extracted in the appropriate energy bands for each of the three detectors, to filter out periods of X-ray background flaring. 0.5–7.0 keV composite images were then created for each source, and were visually examined for point sources. These were excised from further spectral analysis.

4 COOLING TIME PROFILES

4.1 Spectral analysis

In order to obtain radial cooling time profiles, we first need radial temperature and electron number density profiles of the individual groups and clusters of our parent sample. In order to extract spectra, we generated a series of concentric annuli for each source. All annuli for the same source were defined in such a way to ensure that they all had the same number of counts in them, or signal-to-noise ratio. The

signal-to-noise ratio of, or number of counts in, the annuli of a source was defined by the quality of the available data for the source in question. We followed the standard CIAO and SAS routines for the generation of source and background spectra, ancillary region files (ARFs) and redistribution matrix files (RMFs) for sources with *Chandra* and *XMM-Newton* data, respectively. To take projection effects into account, the spectra were deprojected using the DSDE-PROJ code (Sanders & Fabian 2007). All spectral fits were performed in XSPEC (Arnaud 1996) v12.7.1b. For further details on our spectral analysis and fitting, we refer the reader to Section 4.1 of Paper I.

We note that we were not able to extract deprojected profiles from all the sources in our parent sample. This is because the data quality was not always sufficient to give reliable deprojected temperature and electron number density profiles. For this reason, we did not perform any further spectral analysis, such as calculation of a cooling time profile, on these sources. We were able to extract reliable deprojected profiles for 65 sources out of the 101 sources in our parent sample, and these sources are listed in tables 1 and 3 of Paper I (indicated by an asterisk next to their name). We did however search for X-ray cavities in all the sources in our parent sample (see Section 5), and list the sources that do or might harbour cavities in Table 2. We point out that Table 1 only contains sources for which we were able to reliably obtain a deprojected number density and temperature profile, and hence calculate a central cooling time.

4.2 Deprojected cooling time profiles

Having obtained deprojected radial temperature and electron number density profiles for 65 out of 101 of the groups and clusters in our parent sample, as previously mentioned in Section 2.1, we were able to calculate individual cooling time profiles. These were calculated using the method described in Section 4.2 of Paper I, and are included in the overall cooling time profile in the right-hand panel of figure 2 in the same paper. These individual cooling time profiles were calculated in order to obtain a rough idea of the cooling behaviour of the clusters and groups in our parent sample. However, the equations used in that paper provide only a crude approximation of the cooling behaviour of the sources in our subsample, as they assume solar abundances. In order to calculate the central cooling times of each source in our subsample, we follow the method described below.

The cooling time, t_{cool} , of a gas parcel with a total number density n_t , temperature T and emissivity ϵ is given by

$$t_{\text{cool}} = \frac{\frac{5}{2} n_t k_B T}{\epsilon}. \quad (1)$$

Using the definition of the normalisation, A , of the APEC or VAPEC component from XSPEC,

$$A = \frac{10^{-14}}{4\pi[D_A(1+z)]^2} \int n_e n_H dV, \quad (2)$$

Equation 1 can be rewritten as

$$t_{\text{cool}} = \frac{5}{2} \times \frac{27}{14} \times \sqrt{\frac{14\pi 10^{14}}{3}} \times D_A(1+z) \frac{\sqrt{AV} k_B T}{L_X}, \quad (3)$$

where D_A is the angular diameter distance to the source, z is the source redshift, n_e and n_H are the electron and

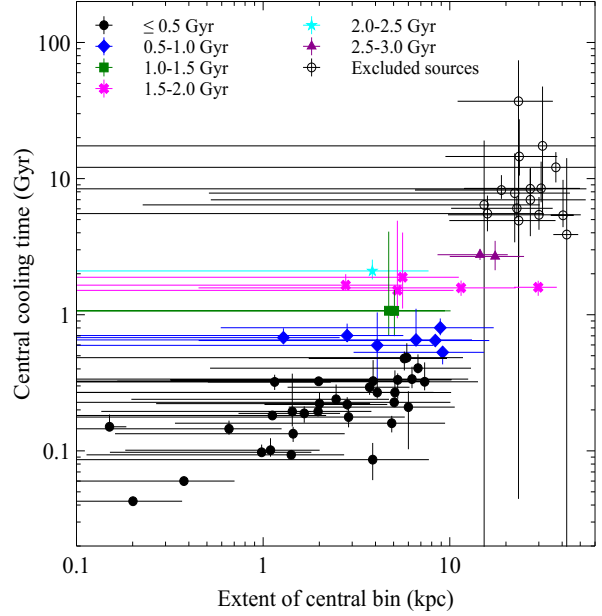


Figure 2. Central cooling time vs. extent of the central spectral bin for the 65 sources in our parent sample, for which we have obtained central cooling time measurements. The different filled symbols indicate sources belonging to different central cooling time bins, while the empty circles indicate the 16 excluded sources.

hydrogen number densities respectively, V is the volume of the gas parcel and L_X is its luminosity. The temperature T , luminosity L_X and normalisation A were obtained from the spectral fits. Since we obtain the aforementioned values from the spectral fitting, no assumptions about the gas abundance were necessary. We have used

$$n_H = \frac{6}{7} n_e, \quad (4)$$

and

$$n_t = \frac{27}{14} n_e. \quad (5)$$

The two above equations were calculated by ignoring contributions from all elements other than hydrogen and helium, and assuming mass fractions of 75 and 25 percent, respectively. We have also assumed that helium and hydrogen are both fully ionised.

For the sources in our short central cooling time subsample, the resulting central cooling times are shown in column 8 of Table 1. The central cooling times are plotted against the extent of the corresponding central spectral bin in Fig. 2, for the 65 sources for which we were able to obtain reliable central cooling time estimates. The different symbols represent systems in different central cooling time bins (see Table 1), and the empty symbols indicate the 16 excluded sources. We point out that the x-axis of Fig. 2 is effectively the mean radius of each spectral bin, and the horizontal error bars are its radial extent.

It is clear that there is a weak trend between the central cooling time calculated here, and the radial extent covered by the central spectral bin. However, there are sources with

central spectral bins of a similar size, that have significantly different central cooling times. There are a few exceptions to this, notably the two sources indicated by the purple triangles, which are included in our short central cooling time subsample, and the excluded sources. Therefore, we do not expect our estimates of the central cooling time to be noticeably affected by our choice of spectral bin size. Rather, it seems that calculations of the central cooling time are more strongly affected by the count rate within the central 20 kpc of each source (see Section 2.1 and Fig. 1), which is an intrinsic property of each source. From the right hand panel of Fig. 1, we can see that there is a spread of more than an order of magnitude in the count rate, of the sources that have a central cooling time ≤ 3 Gyr. In fact, if the central cooling time was defined as the cooling time of the gas at a certain radius from the source centre, for example at 1 kpc as is done in Birzan et al. (2012), the central cooling time of sources whose innermost bins are centered at a distance greater than 1 kpc, is likely to have stayed the same, or even increased due to the poorer data quality, which leads to noisier deprojected spectra. On the other hand, for sources with better resolved central regions, again the central cooling time would either stay the same, or increase due to the inclusion of regions at distances larger than those covered by the central spectral bin. This is based on the shape of the overall cooling time profile, shown in fig. 2 of Paper I, which gives an indication of the general cooling time behaviour of the sources in the parent sample.

We note that, in Fig. 2, there are some sources whose central spectral bin does not cover the innermost regions of the core (i.e. the spectral bin does not go down to, in this case, 0.1 kpc or less). This is either due to the presence of a central point source, which was excised during the spectral analysis, or, less often, because the deprojection of the inner core regions did not give reliable temperature and electron number density estimates. We point out that the longer central cooling time calculated for the 16 excluded sources is not entirely due to resolution effects, as there are sources in our short central cooling time subsample which have central bins of a similar size to that of the 16 excluded sources.

5 IMAGING ANALYSIS

5.1 X-ray cavity detection

As previously mentioned, the main aim of this paper is the study of the cavity dynamics of a sample of X-ray groups and clusters. We thus employ unsharp-masking to detect cavities in all the sources of our parent sample, not just those in our short central cooling time subsample. The way unsharp-masking works is the same image is smoothed twice, once with a wider smoothing kernel, and then with a less wide kernel. The more heavily-smoothed image is then subtracted from the less-smoothed image, thus revealing small-scale inhomogeneities in the image, such as X-ray cavities. In our analysis, we smoothed 0.5–7.0 keV background-subtracted, exposure-corrected *Chandra* images with 1-, 2-, 8- and 10-pixel Gaussians. We then subtracted each of the two more heavily-smoothed images from each of the less-smoothed images. The 0.5–7.0 keV background-subtracted, exposure-corrected images and the unsharp-masked images are pre-

sented in Fig. A1 of Appendix A. We only show the unsharp-masked image that best highlighted the presence of X-ray cavities, which for most sources, is the subtraction of the 8-pixel Gaussian smoothed image from the 2-pixel Gaussian smoothed image.

We classify sources as having certain (“C”), possible (“P”) or no cavities (“N”), based on the following classification scheme:

- Sources with **certain** cavities. The cavities are (a) clearly visible in the original image (i.e. background-subtracted and exposure-corrected image), as well as the unsharp-masked image, or (b) are unambiguously visible in the unsharp-masked image.
- Sources with **possible** cavities. These cavities are either (a) hinted at in the original image, but not clearly visible in the unsharp-masked image, or (b) visible in the unsharp-masked image, but the data are too noisy for the presence of a cavity to be certain. Cavities visible only in the unsharp-masked image are listed as only possible because, what might appear like a cavity, may be a conveniently located and shaped surface brightness depression, which is actually an artefact of the unsharp-masking.
- Sources with **no** cavities. In this case, both the original and unsharp-masked image show no visual sign of an X-ray cavity. Included in this category are sources in whose unsharp-masked image, the surface brightness depression forms a dark annulus about the source centre. This dark annulus is most likely an artefact introduced by the unsharp-masking, through the presence of a sharp central brightness excess.

Table 2 lists all the sources which display certain or possible cavities, along with the size of the cavities and the distance from their centre to the centre of their host group or cluster, both of which were calculated from the unsharp masked images. Here, we have assumed that the cavities are prolate ellipsoids, with a semimajor axis along the direction of the jet r_a , and a semimajor axis perpendicular to the jet direction, r_b . We also indicate whether there is extended H α filamentary structure in the core of each source, along with the relevant reference. The “?” in the cases of NGC 499 and NGC 777 indicates that we were unable to find any evidence from the literature, which supported the presence or absence of H α filaments in these sources. All the sources that have certain or possible X-ray cavities also have a central cooling time of ≤ 3 Gyr. Hence, out of the 49 sources in our subsample, a maximum of 30 of them display X-ray cavities (~ 61 percent). We note that there are a few sources with short central cooling times that do not show any signs of X-ray cavities. These sources are the starred sources in Table 1.

Through our search for X-ray cavities using unsharp-masking, we have uncovered some previously undiscovered cavities in some sources in our sample. These newly-discovered cavities are the cavity in NGC 3402, the “possible” cavity in Abell 1644 and the eastern ghost cavity in NGC 5846. A ghost cavity to the west of the centre of NGC 5846 has been reported previously by Machacek et al. (2011), though the same authors do not detect a cavity to the east. A cavity has not been previously detected in NGC 3402 or Abell 1644.

Source name (1)	Group/cluster (2)	Cavity location (3)	r_a (kpc) (4)	r_b (kpc) (5)	Distance from core (kpc) (6)	Cavity classification (7)	H α filaments (8)
2A0335+096	Cluster	NW	15.0	6.7	43.9	C	yes (a)
		NW	11.6	9.1	35.9	C	"
		N	6.5	13.0	66.3	C	"
NGC 4472	Group	E	1.3	0.8	3.2	C	no (c, i)
		W	1.3	0.9	3.9	C	"
NGC 4696	Cluster	E	1.7	3.0	3.0	C	yes (d)
		W	1.6	2.8	3.1	C	"
A 262	Cluster	E	3.5	3.4	7.5	C	yes (f)
		W	4.1	3.4	6.5	C	"
HCG 62	Group	N	2.1	2.8	7.5	C	no (g)
		S	2.7	2.4	5.2	C	"
NGC 1399	Cluster	N	2.1	1.3	5.0	C	no (h, i)
		S	2.2	1.7	6.4	C	"
NGC 4636	Group	E	1.5	1.4	3.4	C	yes (i)
		NW	1.2	1.8	3.6	C	"
		SW	1.8	1.9	4.9	C	"
NGC 5044	Group	N	3.8	3.5	5.7	C	yes (h)
		S	3.3	4.4	8.3	C	"
		E	2.8	3.5	7.5	C	"
		W	2.7	1.3	4.1	C	"
NGC 5813	Group	NE	0.8	0.4	1.4	C	yes (h)
		NE	1.6	1.3	4.0	C	"
		NE	4.2	6.2	14.2	C	"
		SW	0.6	0.7	1.5	C	"
		SW	3.1	3.1	6.5	C	"
NGC 6338	Cluster	SW	3.1	3.6	6.3	C	yes (j)
		NE	3.6	2.8	5.5	C	"
A 1991	Cluster	N	5.0	15.5	12.9	C	yes (k)
		S	4.4	6.7	10.7	C	"
IC 1262	Group	N	4.0	7.3	8.3	C	yes (l)
A S1101	Cluster	SE	4.7	7.4	14.8	C	yes (m)
A 133	Cluster	NW	7.0	8.4	19.4	C	yes (n)
		SW	7.5	9.9	24.3	C	"
A 85	Cluster	S	4.6	7.9	13.9	C	no (n)
A 1795	Cluster	N	5.8	16.7	10.6	C	yes (o)
A 2052	Cluster	N	4.7	7.1	8.3	C	yes (o)
		N	3.2	10.3	18.2	C	"
		S	4.9	13.1	8.1	C	"
		S	4.3	7.0	19.9	C	"
A 2199	Cluster	E	6.9	5.3	16.8	C	no (p)
		W	8.9	6.9	23.4	C	"
A 4059	Cluster	N	14.2	17.9	22.6	C	yes (n)
NGC 1550	Group	SE	2.1	3.0	8.5	C	no (l)
NGC 3402	Group	SW	1.6	1.4	3.6	C	no (k)
Hydra A	Cluster	NE	11.8	11.3	25.9	C	yes (n)
		NE	35.6	39.7	83.1	C	"
		SW	13.4	12.7	26.9	C	"
		SW	34.6	36.6	109.2	P	"
A 3581	Cluster	E	2.4	2.5	4.9	C	yes (b)
		E	2.2	4.5	12.9	C	"
		W	3.1	3.3	4.3	C	"
		W	3.3	7.6	22.8	P	"
MKW3s	Cluster	SW	13.5	6.7	58.6	C	yes (q)
		S	16.9	15.4	68.2	P	"
NGC 5846	Group	S	0.4	0.9	0.7	C	yes (e)
		N	0.4	0.8	1.0	C	"
		E	1.2	1.3	5.0	P	"
		W	1.7	1.5	5.5	P	"
NGC 4325	Group	E	2.4	4.6	11.8	P	yes (o)
		W	2.6	4.3	7.7	P	"
A 1644	Cluster	S	8.3	6.1	15.0	P	yes (n)
A 496	Cluster	N	5.6	4.9	14.2	P	yes (n)
		S	2.8	7.9	7.1	P	"
NGC 499	Group	SE	1.4	2.0	4.5	P	?
		SW	1.1	1.3	3.0	P	"

Table 2 – *continued*

Source name (1)	Group/cluster (2)	Cavity location (3)	r_a (kpc) (4)	r_b (kpc) (5)	Distance from core (kpc) (6)	Cavity classification (7)	H α filaments (8)
NGC 777	Group	E	1.9	2.3	4.6	P	?
		W	2.1	2.4	4.0	P	"

List of the properties of the X-ray cavities of the groups and clusters in our sample, all of which are also part of the short central cooling time subsample. All the sources are also part of the short central cooling time subsample. “C” denotes sources with certain cavities, while “P” indicates sources with possible cavities. We were unable to find evidence in the literature supporting either the presence or absence of H α filaments in NGC 499 and NGC 777, which we indicate with “?” in the relevant column. (1) source name, (2) group/cluster classification of source, (3) location of X-ray cavity, (4) length of axis along the direction of the jet in kpc, (5) length of axis perpendicular to the jet in kpc (6) distance of cavity from source centre, (7) classification of X-ray cavities as certain (C) or possible (P) (for more details, see Section 5), and (8) presence/absence of H α filaments and corresponding reference. REFERENCES.- (a) Romanishin & Hintzen (1988), (b) Canning et al. (2013), (c) Arrighi Battaia et al. (2012), (d) Crawford et al. (2005), (e) Goudfrooij & Trinchieri (1998), (f) Plana et al. (1998), (g) Valluri & Anupama (1996), (h) Goudfrooij et al. (1994), (i) Werner et al. (2014), (j) Martel et al. (2004), (k) McDonald et al. (2011), (l) Crawford et al. (1999), (m) Jaffe et al. (2005), (n) McDonald et al. (2010), (o) McDonald et al. (2012), (p) Godon et al. (1994), (q) Edwards et al. (2009).

5.1.1 XMM-Newton images

We note that there are some sources in our sample, for whose analysis *XMM-Newton* data were used. These are Abell 1736, Abell 2192, Abell 2197, Abell 3376, Abell 3390, Abell 3391, Abell 3395, Abell S0405, Abell S0805, IC 4296, IC 4329, NGC 410, RXCJ0920.0+0102, RXCJ1840.6-7709, RXCJ2314.7-0222 and UGC 4052. To search these sources for cavities, we used only the cleaned (i.e. periods of background flaring have been removed) EPIC MOS data. We excluded the pn detector from our imaging analysis as it has numerous detector gaps in its centre, which is where we are most likely to see X-ray cavities. We generated 0.5–7.0 keV images for each MOS detector separately, and then added these together. The total image was then smoothed with 1-, 2-, 8- and 10-pixel Gaussians, as was done with the *Chandra* data. Each of the two more heavily smoothed images were then subtracted from each of the less smoothed images. The total image of each source, and one of the unsharp-masked images, are shown in Fig. A2 of Appendix A. We did not discover X-ray cavities in any of the aforementioned sources, which may be in part due to the poorer angular resolution and larger point spread function (PSF) of the EPIC instruments. We note that the data for Abell 2197 were so heavily contaminated by background flaring, that no usable exposure time was left after removing periods of background flaring. We show no combined MOS image for IC 4329, as the object in the centre of the detectors is a very bright FR-I source, and so the MOS detectors were operated in large window mode. This means that the diffuse emission from the cluster is not visible in the images.

5.2 Sources without X-ray cavities

To verify that we are not “missing” any X-ray cavities, that happen to be too small or faint to be readily visible in the currently available data, we estimated the size of X-ray cavities necessary to offset cooling in the cores of some of the sources in our sample. We performed this calculation for the three sources in our sample which have a central cooling time ≤ 0.25 Gyr, and which do not have cavities, namely MKW4, NGC 533 and NGC 6482. We assumed that the cavities are spherical in shape, that they are produced in pairs and that

they move and expand at the local sound speed. We determined the size of the bubbles needed to offset the cooling within the cooling radius, r_{cool} (the radius within which the cooling time is ≤ 3 Gyr), and we used the results from the spectral fitting to estimate the local sound speed.

We find that if the X-ray cavities for the three sources were located close to the centre of the host source, only the cavities in MKW4 would be just about large enough to be resolved in the currently available observations. However, not knowing the size or location of these bubbles significantly decreases the possibility of their detection, as does the fact that they may not have bright rims. We note that previous searches for X-ray cavities in these sources have not found them either (Dong et al. 2010; Khosroshahi et al. 2004; Gu et al. 2012).

6 RESULTS

6.1 Clusters vs. groups

To inspect if there is any difference in the distribution of sources with X-ray cavities with respect to their central cooling time, we examine the groups and clusters in our subsample separately. The central cooling time is defined as the cooling time calculated for the gas in the innermost spectral bin of each source. In addition, we used 0.5 Gyr bins for the central cooling time, covering the 0–3.0 Gyr range. The distributions for the groups and the clusters of our subsample are given in the left-hand and right-hand panels of Fig. 3, respectively. The areas enclosed within the dashed rectangles represent the total number of groups or clusters in each bin, and the blue shaded regions indicate the number of groups or clusters that harbour X-ray cavities. We point out that all the sources from our main sample of 101 X-ray groups and clusters that have X-ray cavities, also have a central cooling time of ≤ 3 Gyr.

It is obvious from Fig. 3 that the vast majority of the subsample sources lie in the ≤ 0.5 Gyr bin. In fact, 32 out of 49 sources (~ 65 percent) of the short central cooling time subsample, are in this central cooling time bin. The number of both groups and clusters in longer central cooling time bins decreases quite rapidly. From Fig. 3, we can state that

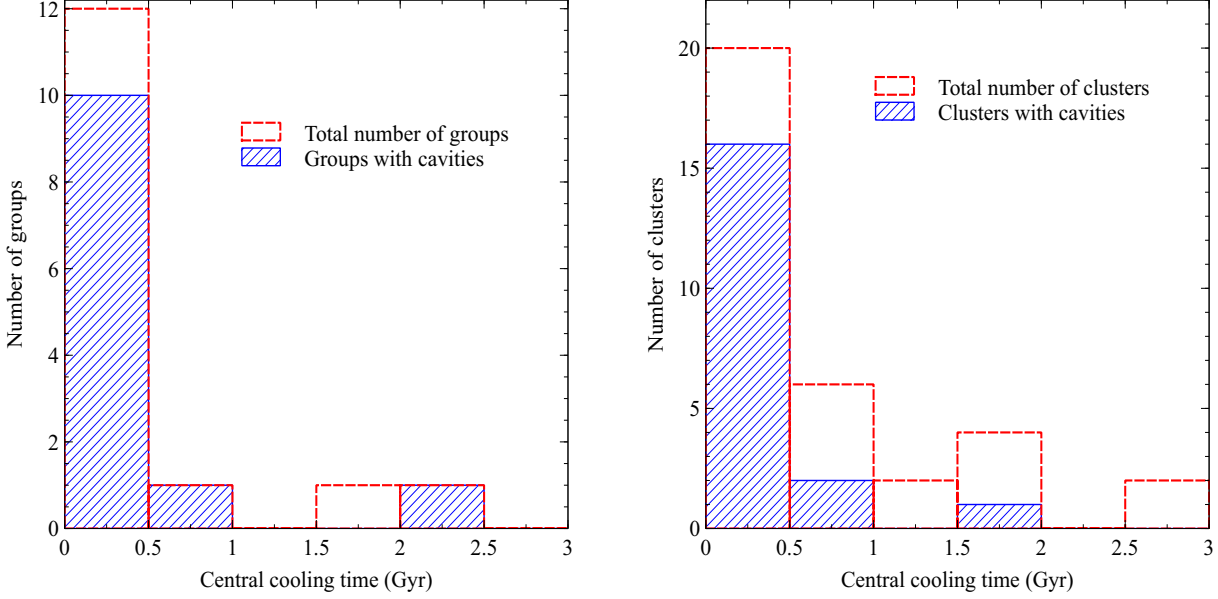


Figure 3. The distribution of groups (left panel) and clusters (right panel) in our subsample, and whether they have cavities or not, with respect to their central cooling time. The dashed rectangular areas indicate the total number of groups or clusters, while the blue shaded areas represent the number of groups or clusters that do have cavities.

the AGN duty cycle of the groups and clusters with a central cooling time of ≤ 3 Gyr is $\simeq 61$ percent. However, given the added difficulty of detecting bubbles which are not visible due to projection effects, and the fact that almost all of the sources in our subsample have a detected radio source, the actual duty cycle is likely to be much higher.

In the ≤ 0.5 Gyr central cooling time bin, 10 out of 12 groups have cavities (~ 83 per cent), while 16 out of 20 clusters have cavities (80 per cent). This means that the AGN duty cycle for groups and clusters in our subsample, with central cooling times ≤ 0.5 Gyr, are quite similar. Fig. 3 also indicates that most sources with short central cooling times harbour X-ray cavities. In other words, the majority of sources in which heating is needed to offset cooling, possess X-ray cavities. However, there are significantly fewer groups and clusters that have X-ray cavities with central cooling times longer than 0.5 Gyr, so it is not easy to extrapolate this conclusion for longer central cooling times.

6.2 Data quality effects

The detectability of X-ray cavities in a X-ray group or cluster could be strongly dependent on the quality of the data available on that source. To test whether the lack of data on a source impacts the detection of cavities, we calculated the number of counts within the central 20 kpc of each source in our short central cooling time sample. We use 0.5–7.0 keV images from which point sources have been removed, and that have not been exposure-corrected (in the case of *Chandra* data, the images have been background-subtracted). If a central point source is visible at the core of a group or cluster, we exclude it from the calculation. We point out that in the case of some of the lowest redshift sources, a circle with a radius of 20 kpc extends beyond the area of the ACIS-I

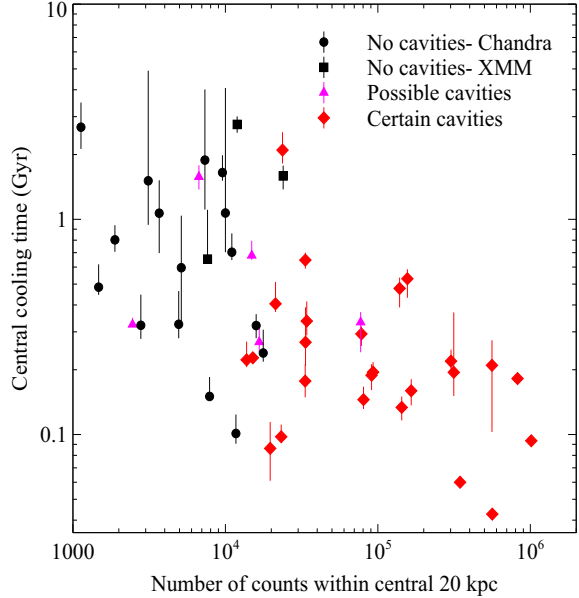


Figure 4. Central cooling time vs. total number of counts within the central 20 kpc of each source in the short central cooling time subsample, adapted from Fig. 4. The black circles and squares represent sources with no cavities, for whose analysis *Chandra* and *XMM-Newton* data were used, respectively. The pink triangles indicate sources all of whose cavities are classified as “possible”, while the red diamonds are the sources which have at least one “certain” cavity. The rightmost black square is RXCJ1840.6-7709, which has a very bright source at its core.

and ACIS-S chips. In addition, there are three sources for which we have used *XMM-Newton* data, all three of which do not have X-ray cavities. These three sources will have a higher number of counts in their central 20 kpc due to the combination of detectors, and the higher sensitivity of the EPIC detectors compared to the ACIS detectors.

We plot the central cooling time of each source against the corresponding number of total counts within 20 kpc in Fig. 4. This figure is similar to the left hand panel of Fig. 1, but here we have not included the “excluded” sources of Fig. 1. In addition, we have colour-coded the 49 remaining sources (i.e. the sources in the short central cooling time subsample), according to the detection or non-detection of an X-ray cavity. The sources with no cavities, for which we used *Chandra* or *XMM-Newton* data in the analysis, are represented by the black circles and squares, respectively. Sources whose cavities have all been classified as “possible”, or that have at least one “certain” cavity, are indicated by the pink triangles and red diamonds, respectively. The right-most black square is RXCJ1840.6-7709, which has a very bright source at its core, and as such has a high number of counts (see Appendix A for the relevant *XMM-Newton* image). It is evident that the sources which are found to have X-ray cavities generally have the highest number of counts and shortest cooling times, due to their cores being better resolved. In fact, with just a couple of exceptions, sources with fewer than ~ 20000 counts within a 20 kpc radius circle from their core, do not have clearly detected X-ray cavities. Therefore, the values obtained from Fig. 3 should be regarded as lower limits, pending the availability of longer observations. Deeper observations will reveal more cavities in these sources, and raise the fraction of sources with cavities towards unity, reaffirming the fact that the incidence of cavities is underestimated.

The inverse trend seen in Fig. 4 is likely a signal-to-noise ratio effect.

6.3 Cavity size vs. temperature

To examine whether there is any correlation between the size of cavities in a group or cluster, and the temperature of the host group or cluster, we plot the size of the cavity against the deprojected temperature. Specifically, we examine the correlation between cavity size and the deprojected temperature at the location of the cavity within its host group or cluster. Since we have modelled the cavities in our sample as prolate ellipsoids, we use the average of r_a and r_b as a proxy for the cavity “radius”, r . The resulting plot is shown in Fig. 5. The black circles represent the inner (or only) set of cavities in a source, and the red squares represent the outer set of cavities. The two blue diamonds are the middle set of cavities in NGC 5813. The dotted line and dot-dashed line in the same figure indicate the relations $r \propto T^{0.5}$ and $r \propto T^2$, respectively, though neither is a fit to the data. As can be seen, the size of an X-ray cavity does not have a fixed dependence on the ambient ICM temperature.

We now explore the relation between the radius of a bubble, r , and the temperature of the ICM at its location, T_{ICM} . From Churazov et al. (2000), we have

$$r \propto \sqrt{\frac{P_{\text{cav}}}{\rho v_K}}, \quad (6)$$

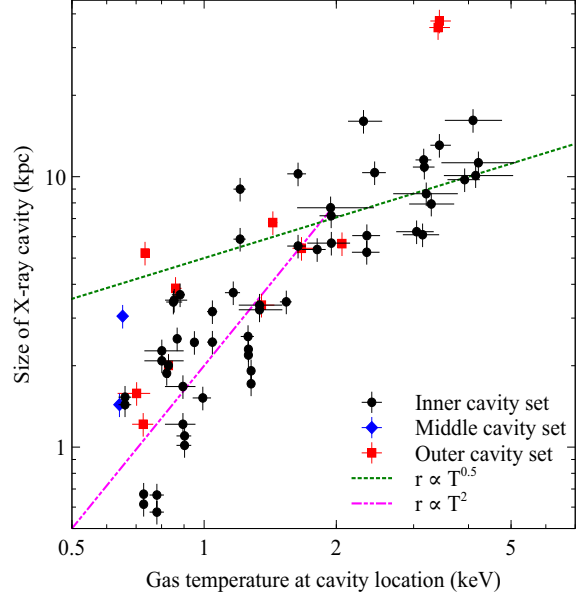


Figure 5. X-ray cavity size vs. gas temperature at the cavity location. The inner (or only) set of cavities in a source, and the outer set of cavities are symbolised by the black circles and red squares, respectively. The blue diamonds represent the middle set of cavities in NGC 5813. The dotted line represents the relation $r \propto T^{0.5}$, while the dot-dashed line indicates $r \propto T^2$.

where P_{cav} is the power inflating the cavity, p is the pressure of the surrounding ICM (we assume that the cavity is almost in pressure equilibrium with its surrounding gas), and v_K is the Keplerian velocity at the location of the cavity. The Keplerian velocity is comparable to the local sound speed, c_s , in the ICM, so

$$v_K \simeq c_s \propto T_{\text{ICM}}^{1/2}. \quad (7)$$

For a limited range of cooling times, the Bremsstrahlung cooling time of the ICM gas, t_{Brem} , is given by

$$t_{\text{Brem}} \propto \frac{T_{\text{ICM}}^{1/2}}{n}, \quad (8)$$

where n is the number density of the ICM gas. From this relation, we have $n \propto T_{\text{ICM}}^{1/2}$. Combining this with the ideal gas law, $p = nk_B T_{\text{ICM}}$, where k_B is the Boltzmann constant and p is the pressure of the ICM gas, we have $p \propto T_{\text{ICM}}^{3/2}$, for a limited range of Bremsstrahlung cooling times. The power inflating the cavity depends directly on the cooling luminosity of the cluster, L_{cool} , as $P_{\text{cav}} \propto L_{\text{cool}}$, which in turn depends on the bolometric luminosity, L_{bol} , as $L_{\text{cool}} \propto L_{\text{bol}}$ (Peres et al. 1998). For clusters, it is well-established that $L_{\text{cool}} \propto T_{\text{ICM}}^3$ (e.g. Markevitch 1998; Pratt et al. 2009; Maughan et al. 2012).

By substituting all the above scaling relations into Equation 6, we get

$$r \propto T_{\text{ICM}}^{0.5}. \quad (9)$$

This relation fits the general trend of the points in Fig. 5 with $T_{\text{ICM}} \geq 1.5$ keV reasonably well, though there is significant scatter. On the other hand, below 1.5 keV, this scaling relation no longer applies, and the scatter is much greater.

This could be due to the fact that, below 1.5 keV, the relation between the X-ray luminosity and the temperature of the ICM is much less well-constrained, as has been observed by e.g. Osmond & Ponman (2004). The scatter in Fig. 5 may be reflecting this. We have overplotted the $r \propto T_{\text{ICM}}^2$ relation in the same figure to indicate this discrepancy, though this relation is not a fit to the data.

6.4 Cavity power vs. cooling luminosity

As mentioned in Section 1, outbursts of energy from the brightest cluster galaxy (BCG) AGN are thought to be the main mechanism quenching cooling flows in groups and clusters of galaxies. To check whether this is the case with the groups and clusters in our subsample, we calculated the power of all the cavities in our subsample, P_{cav} , and the cooling luminosity, L_{cool} , of the corresponding groups and clusters. We use

$$P_{\text{cav}} = \frac{4p_{\text{th}}V}{t_{\text{cav}}}, \quad (10)$$

where p_{th} is the thermal pressure of the gas surrounding the cavity, V is the volume of the cavity, and t_{cav} is the age of the cavity. As the X-ray cavities are assumed to be prolate ellipsoids, with r_a and r_b the semimajor axes along and perpendicular the jet direction respectively, the volume V is

$$V = \frac{4}{3}\pi r_a^2 r_b. \quad (11)$$

Here, we have assumed that the gas in the X-ray cavities is in pressure equilibrium with the surrounding ICM, and the age of the cavity is defined as the time it would take the cavity to reach its current location at the speed of sound

$$t_{\text{cav}} = \frac{R}{c_s}, \quad (12)$$

where R is the distance of the centre of the cavity from the centre of the source, and c_s is the local speed of sound. The latter is defined as

$$c_s = \sqrt{\gamma \frac{k_B T}{\mu m_H}}, \quad (13)$$

where γ is the adiabatic index for the gas, m_H is the mass of the hydrogen atom, and μ is equal to 0.62. Here we have used $\gamma=5/3$ for a non-relativistic gas. We use this definition for the age of the cavity, as no strong shocks have been detected in groups or clusters. Therefore, the bubbles cannot be expanding at a speed much greater than the local sound speed in the ICM. We note that other studies (e.g. Birzan et al. 2004) have also used the buoyancy rise time and cavity refill time (the amount of time it would take to refill the displaced volume as the cavity rises outwards) to calculate the age of a cavity, in addition to using the local sound speed. The resulting values for the cavity ages using these different methods do not vary significantly, and therefore our results would not be affected if we used the other cavity age estimates. The cooling luminosity L_{cool} is calculated from the spectral fits, for which a WABS*APEC model was used in XSPEC, and is defined as the luminosity of the gas within the cooling radius r_{cool} . In turn, r_{cool} is defined as the radius within which the gas has a cooling time of ≤ 3 Gyr, in line with previous studies (Dunn & Fabian 2006, 2008). As we are studying a

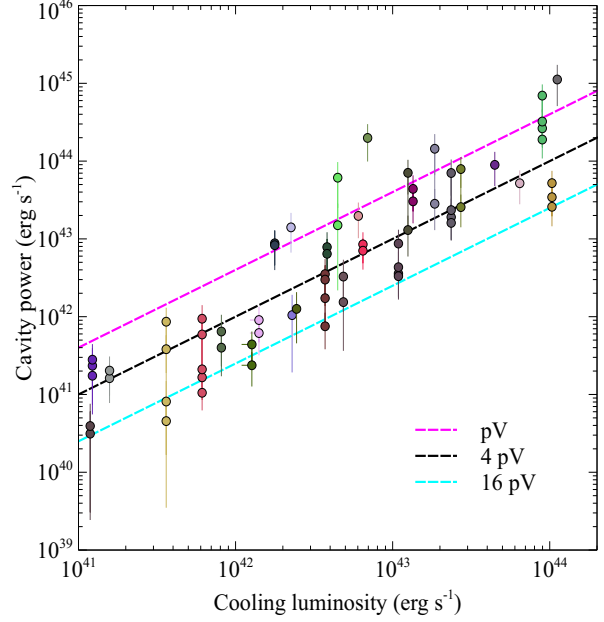


Figure 6. Cavity power vs. cooling luminosity for the 42 groups and clusters in our sample. The pink, black and blue dashed lines show equality for pV , $4pV$ and $16pV$, respectively. The cavities of each source have been given the same colour.

sample of relatively nearby galaxy groups and clusters, our selection of cooling radius ensures we are able to study the innermost regions of these sample sources and take advantage of the higher spatial resolution offered, and so study AGN feedback in more detail. We have assumed a typical 20 percent error on the cavity dimensions, and the errors on P_{cav} were calculated using standard error propagation. The resulting plot is shown in Fig. 6, where the bubbles of each source have been given the same colour. The pink, black and blue dashed lines represent equality for cavity energies of pV , $4pV$ and $16pV$, respectively.

As can be seen from Fig. 6, the X-ray cavities of most sources lie between the pV and $16pV$ lines, rather than above the pV line or below the $16pV$ line. This indicates that the “bubbling mode” of the central AGN has to be a fairly continuous process in order to offset cooling, rather than the result of an episodic outburst of AGN activity, which was triggered by an accretion event. However, there are a few sources which cannot offset the cooling flow in their cores through current AGN heating alone. These results from our analysis are in agreement with those of Birzan et al. (2012), who found that the systems with bubbles in the sample they use require a constant input of energy from the AGN (see figure 5 of the same paper). Our results also agree with recent theoretical work on AGN feedback, which favour relatively gentle and self-regulated AGN feedback, rather than feedback manifested in sudden and violent outbursts (see e.g. Gaspari et al. 2011, 2012). Fig. 6 is, however, in tension with the results of Nulsen et al. (2007, 2009), who study a sample of nearby elliptical galaxies. The same authors find that cooling in these systems can be offset by intermittent AGN outbursts, rather than continuous bubbling activity.

We note that Birzan et al. (2012) define the cooling radius, r_{cool} as the radius within which the cooling time of the gas is 7.7 Gyr (we use 3 Gyr in our analysis). In addition, they study the correlation between cavity power and cooling luminosity for two subsamples of sources harbouring cooling flows: both subsamples require sources to have a separation ≤ 12 kpc between the optical core and the X-ray emission peak, but the first subsample additionally requires that $\eta_{\text{min}} \leq 5$ (η_{min} is a measure of the gas' thermal stability; see Voit et al. 2008), while the second requires a cooling time of 0.5–1 Gyr at 1 kpc. It is encouraging to see our results agree with those of Birzan et al. (2012), despite the differences in the subsample selection and the definition of r_{cool} .

6.5 Do smaller or larger bubbles travel faster?

In our study, there are a number of sources that have multiple sets of bubbles, which increase in size with increasing distance from the source centre, such as Hydra A and NGC 5813. Here we examine whether these outer, larger bubbles are a result of the merging of individual smaller bubbles, produced in separate bubbling events.

Diehl et al. (2008) showed that bubbles seen at larger distances from the cores of a sample of clusters, appear to be a lot larger than those at smaller radii. In fact, these outer bubbles are larger than expected even from simple adiabatic expansion, which is puzzling. An example of a multicavity system which has been studied in detail is Hydra A, in which Wise et al. (2007) identify 3 sets of bubbles, which show a steep increase of bubble radius with distance from the cluster core. It is therefore possible that these larger outer bubbles are due to the accumulation and merging of individual bubbles, that were created in multiple AGN cycles. Indeed, features that correspond to drops in flux in X-ray images, and could be due to the merging of many smaller individual cavities, have been seen in e.g. the Perseus cluster (Fabian et al. 2011) and Abell 2204 (Sanders et al. 2009). After calculating the mechanical power necessary to create the outermost, and largest, set of bubbles in these clusters in a single AGN outburst, both authors conclude it is more likely that these bubbles are the result of the accumulation of many smaller bubbles produced during past AGN outbursts, rather than by a single outburst. In particular, Fabian et al. (2011) conclude that bubbles must be long-lived, and that faster-moving bubbles rise and sweep up slower-rising bubbles, merging with them. It is thought that bubbles become detached from the AGN jet, rise buoyantly outwards from the cluster centre, and become “trapped” at some larger radius. There, it is possible that they are neutrally buoyant, either through mixing with the surrounding ICM gas, or through interactions with the local magnetic fields, which arrest their upward movement. A question which then arises is whether small bubbles catch up with previously created larger bubbles, or vice versa. In other words, do smaller or larger bubbles travel faster through the ICM?

The terminal velocity of a bubble at its current location, assuming it is rising buoyantly through the ICM, is given by (Birzan et al. 2004)

$$v_t \simeq \sqrt{\frac{2gV}{SC}}, \quad (14)$$

where g is the gravitational acceleration, V is the volume of the bubble, S is its cross section and $C=0.75$ is the drag coefficient (Churazov et al. 2001). The gravitational acceleration g can be calculated using the stellar velocity dispersion of the central galaxy of a group or cluster, σ , and, assuming that this galaxy is an isothermal sphere, is defined as (Binney & Tremaine 1987)

$$g \simeq \frac{2\sigma^2}{R}, \quad (15)$$

where R is the projected distance from the centre of the group or cluster to the centre of the cavity. Assuming the bubbles are spherical in shape, Equation 14 can therefore be rewritten as

$$v_t \propto \sigma \sqrt{\frac{r}{R}}. \quad (16)$$

For bubbles in the same cluster, the σ term in the above equation can be dropped, so we have $v_t \propto \sqrt{r/R}$. As a result, at a given radius in a certain group or cluster, larger bubbles will travel faster. This means that it is possible for larger bubbles to catch up and merge with smaller bubbles that were created at an earlier time.

6.6 Bubbling-induced metallicity gradients

An increasing number of clusters with central abundance drops is being discovered. Some such clusters are the Centaurus cluster (Panagoulia et al. 2013; Sanders & Fabian 2002), Abell 1644 (Kirkpatrick et al. 2009), the Perseus cluster (Sanders et al. 2004), and Abell 2199 (Johnstone et al. 2002). There are also groups with central abundance dips, such as HCG 62 (Rafferty et al. 2013). One explanation for the central abundance drops, at least in the Centaurus cluster, is that X-ray cavities drag out cool, dusty metal-enriched filaments from the cluster core, to outer regions of the cluster, where the filaments are destroyed, e.g. through sputtering in hot gas (for more details, see Panagoulia et al. 2013). There, the metal-rich dust returns to the X-ray phase and mixes with the local ICM, resulting in an abundance increase. There have also been observations of radio lobes sweeping up molecular gas from cluster cores, which is the case in e.g. Abell 1835 (McNamara et al. 2014). Work is underway to identify the sources that exhibit central abundance drops, as well as X-ray cavities. The results of that analysis will be the subject of a future paper.

7 SUMMARY

We searched for X-ray cavities in a volume- and L_X -limited sample of 101 X-ray groups and clusters. We find cavities in 30 sources, all of which have a central cooling time of ≤ 3 Gyr. We then studied the subsample of 49 sources, which have a central cooling time of ≤ 3 Gyr, which, as mentioned, encompasses all sources with X-ray cavities. We then calculated cooling luminosities, L_{cool} , and the power of the cavities, P_{cav} , for each source with cavities. We study the dependence of the detection of X-ray cavities on the central cooling time and data quality, as well as the relation between cavity power and cooling luminosity, for the sources that harbour cavities. The main results of our analysis are:

- We derive the AGN duty cycle for sources with a central cooling time of ≤ 3 Gyr, and estimate its value at ~ 61 percent. This rises to > 80 percent for sources with a central cooling time of ≤ 0.5 Gyr. Taking projection effects and the fact that almost all these sources have a detected central radio source into consideration, the duty cycle is probably higher. This agrees well with results of previous studies (e.g. Bîrzan et al. 2004, 2012; Dunn & Fabian 2006).

- We detect new cavities in three sources in our sample, namely NGC 3402, Abell 1644 and NGC 5846.

- We find that the ability to detect X-ray cavities, in the sources of our short central cooling time sample, strongly depends on the number of counts available in the core of the source, and hence on the data quality. Sources with fewer than 10000 counts within their central 20 kpc do not have clearly detected X-ray cavities, though all sources with ≥ 30000 counts do.

- For the groups and clusters that have X-ray cavities, the bubbling process has to be, on average, continuous, to stop the gas from cooling and forming stars in group and cluster cores. In other words, we find that intermittent AGN outbursts are not powerful enough to offset cooling, and continuous injection of energy into the ICM, in the form of bubbles, is needed. In some of our sources, the energy contained in the cavities is not enough to quench a cooling flow.

- The size of a cavity, loosely depends on the ambient ICM temperature through the relation $r \propto T^{0.5}$, down to temperatures of about 1.5 keV, below which there is much more scatter.

- The bubbles seen at larger distances from the core of a source may be the result of the merging of multiple smaller bubbles, produced in separate AGN outbursts.

Work is underway to search for and study central abundance drops in the sources that display X-ray cavities. We aim to determine whether these abundance drops can be caused by AGN-induced bubbling activity, and if they are spatially correlated with e.g. dust emission in the infrared.

ACKNOWLEDGEMENTS

EKP acknowledges the support of a STFC studentship. We thank the anonymous referee for helpful comments. EKP thanks Becky Canning for help with H α filament data. JHL is supported by NASA through the Einstein Fellowship Program, grant number PF2-130094.

The plots in this paper were created using *VEUSZ*.¹ This research has made use of the NASA/IPAC Extragalactic Database (NED)² which is operated by the Jet Propulsion Laboratory, California Institute of Technology, under contract with the National Aeronautics and Space Administration.

REFERENCES

Anders E., Grevesse N., 1989, *Geochim. Cosmochim. Acta*, 53, 197

- Arnaud K. A., 1996, in Jacoby G. H., Barnes J., eds, *Astronomical Data Analysis Software and Systems V* Vol. 101 of Astronomical Society of the Pacific Conference Series, XSPEC: The First Ten Years. p. 17
- Arrigoni Battaia F., Gavazzi G., Fumagalli M., Boselli A., Boissier S., Cortese L., et al., 2012, *A&A*, 543, A112
- Binney J., Tremaine S., 1987, *Galactic dynamics*
- Bîrzan L., Rafferty D. A., McNamara B. R., Wise M. W., Nulsen P. E. J., 2004, *ApJ*, 607, 800
- Bîrzan L., Rafferty D. A., Nulsen P. E. J., McNamara B. R., Röttgering H. J. A., Wise M. W., Mittal R., 2012, *MNRAS*, 427, 3468
- Boehringer H., Voges W., Fabian A. C., Edge A. C., Neumann D. M., 1993, *MNRAS*, 264, L25
- Böhringer H., Schuecker P., Guzzo L., Collins C. A., Voges W., Cruddace R. G., Ortiz-Gil A., Chincarini G., De Grandi S., Edge A. C., MacGillivray H. T., Neumann D. M., Schindler S., Shaver P., 2004, *A&A*, 425, 367
- Böhringer H., Voges W., Huchra J. P., McLean B., Giacconi R., Rosati P., Burg R., Mader J., Schuecker P., Simiç D., Komossa S., Reiprich T. H., Retzlaff J., Trümper J., 2000, *ApJS*, 129, 435
- Burns J. O., 1990, *AJ*, 99, 14
- Canning R. E. A., Sun M., Sanders J. S., Clarke T. E., Fabian A. C., Giacintucci S., Lal D. V., Werner N., Allen S. W., Donahue M., Edge A. C., Johnstone R. M., Nulsen P. E. J., Salomé P., Sarazin C. L., 2013, *MNRAS*, 435, 1108
- Choi Y.-Y., Reynolds C. S., Heinz S., Rosenberg J. L., Perlman E. S., Yang J., 2004, *ApJ*, 606, 185
- Churazov E., Brüggen M., Kaiser C. R., Böhringer H., Forman W., 2001, *ApJ*, 554, 261
- Churazov E., Forman W., Jones C., Böhringer H., 2000, *A&A*, 356, 788
- Condon J. J., Cotton W. D., Greisen E. W., Yin Q. F., Perley R. A., Taylor G. B., Broderick J. J., 1998, *AJ*, 115, 1693
- Crawford C. S., Allen S. W., Ebeling H., Edge A. C., Fabian A. C., 1999, *MNRAS*, 306, 857
- Crawford C. S., Hatch N. A., Fabian A. C., Sanders J. S., 2005, *MNRAS*, 363, 216
- Diehl S., Li H., Fryer C. L., Rafferty D., 2008, *ApJ*, 687, 173
- Dong R., Rasmussen J., Mulchaey J. S., 2010, *ApJ*, 712, 883
- Dunn R. J. H., Allen S. W., Taylor G. B., Shurkin K. F., Gentile G., Fabian A. C., Reynolds C. S., 2010, *MNRAS*, 404, 180
- Dunn R. J. H., Fabian A. C., 2006, *MNRAS*, 373, 959
- Dunn R. J. H., Fabian A. C., 2008, *MNRAS*, 385, 757
- Dunn R. J. H., Fabian A. C., Taylor G. B., 2005, *MNRAS*, 364, 1343
- Edge A. C., 2001, *MNRAS*, 328, 762
- Edge A. C., Stewart G. C., Fabian A. C., Arnaud K. A., 1990, *MNRAS*, 245, 559
- Edwards L. O. V., Robert C., Mollá M., McGee S. L., 2009, *MNRAS*, 396, 1953
- Fabian A. C., 1994, *ARA&A*, 32, 277
- Fabian A. C., 2012, *ARA&A*, 50, 455
- Fabian A. C., Sanders J. S., Allen S. W., Canning R. E. A., Churazov E., Crawford C. S., Forman W., Gabany J., Hlavacek-Larrondo J., Johnstone R. M., Russell H. R.,

¹ <http://home.gna.org/veusz/>

² <http://ned.ipac.caltech.edu/>

- Reynolds C. S., Salomé P., Taylor G. B., Young A. J., 2011, *MNRAS*, 418, 2154
- Fabian A. C., Sanders J. S., Allen S. W., Crawford C. S., Iwasawa K., Johnstone R. M., Schmidt R. W., Taylor G. B., 2003, *MNRAS*, 344, L43
- Fabian A. C., Sanders J. S., Ettori S., Taylor G. B., Allen S. W., Crawford C. S., Iwasawa K., Johnstone R. M., Ogle P. M., 2000, *MNRAS*, 318, L65
- Gaspari M., Brighenti F., D’Ercole A., Melioli C., 2011, *MNRAS*, 415, 1549
- Gaspari M., Brighenti F., Temi P., 2012, *MNRAS*, 424, 190
- Gitti M., Brighenti F., McNamara B. R., 2012, *Advances in Astronomy*, 2012
- Gitti M., O’Sullivan E., Giacintucci S., David L. P., Vrtilek J., Raychaudhury S., Nulsen P. E. J., 2010, *ApJ*, 714, 758
- Godon P., Soker N., White III R. E., Regev O., 1994, *AJ*, 108, 2009
- Goudfrooij P., Hansen L., Jorgensen H. E., Norgaard-Nielsen H. U., 1994, *A&AS*, 105, 341
- Goudfrooij P., Trinchieri G., 1998, *A&A*, 330, 123
- Gu J.-H., Xu H.-G., Wang J.-Y., Wang Y., Xu S.-F., Qin Z.-Z., Gu L.-Y., An T., Zhang Z.-L., Lei M., 2012, *Research in Astronomy and Astrophysics*, 12, 63
- Hlavacek-Larrondo J., Fabian A. C., Edge A. C., Ebeling H., Sanders J. S., Hogan M. T., Taylor G. B., 2012, *MNRAS*, 421, 1360
- Ho L. C., Ulvestad J. S., 2001, *ApJS*, 133, 77
- Jaffe W., Bremer M. N., Baker K., 2005, *MNRAS*, 360, 748
- Johnstone R. M., Allen S. W., Fabian A. C., Sanders J. S., 2002, *MNRAS*, 336, 299
- Johnstone R. M., Fabian A. C., Nulsen P. E. J., 1987, *MNRAS*, 224, 75
- Khosroshahi H. G., Jones L. R., Ponman T. J., 2004, *MNRAS*, 349, 1240
- Kirkpatrick C. C., McNamara B. R., Rafferty D. A., Nulsen P. E. J., Bîrzan L., Kazemzadeh F., Wise M. W., Gitti M., Cavagnolo K. W., 2009, *ApJ*, 697, 867
- Loewenstein M., Zweibel E. G., Begelman M. C., 1991, *ApJ*, 377, 392
- Machacek M. E., Jerius D., Kraft R., Forman W. R., Jones C., Randall S., Giacintucci S., Sun M., 2011, *ApJ*, 743, 15
- Magliocchetti M., Brüggén M., 2007, *MNRAS*, 379, 260
- Markevitch M., 1998, *ApJ*, 504, 27
- Martel A. R., Ford H. C., Bradley L. D., Tran H. D., Menanteau F., Tsvetanov Z. I., Illingworth G. D., Hartig G. F., Clampin M., 2004, *AJ*, 128, 2758
- Mauch T., Murphy T., Buttery H. J., Curran J., Hunstead R. W., Piestrzynski B., Robertson J. G., Sadler E. M., 2003, *MNRAS*, 342, 1117
- Maughan B. J., Giles P. A., Randall S. W., Jones C., Forman W. R., 2012, *MNRAS*, 421, 1583
- McDonald M., Veilleux S., Mushotzky R., 2011, *ApJ*, 731, 33
- McDonald M., Veilleux S., Rupke D. S. N., 2012, *ApJ*, 746, 153
- McDonald M., Veilleux S., Rupke D. S. N., Mushotzky R., 2010, *ApJ*, 721, 1262
- McNamara B. R., Nulsen P. E. J., 2007, *ARA&A*, 45, 117
- McNamara B. R., Nulsen P. E. J., 2012, *New Journal of Physics*, 14, 055023
- McNamara B. R., Russell H. R., Nulsen P. E. J., Edge A. C., Murray N. W., Main R. A., Vantyghem A. N. et al., 2014, *ApJ*, 785, 44
- McNamara B. R., Wise M., Nulsen P. E. J., David L. P., Sarazin C. L., Bautz M., Markevitch M., Vikhlinin A., Forman W. R., Jones C., Harris D. E., 2000, *ApJ*, 534, L135
- McNamara B. R., Wise M. W., Murray S. S., 2004, *ApJ*, 601, 173
- McNamara B. R., Wise M. W., Nulsen P. E. J., David L. P., Carilli C. L., Sarazin C. L., O’Dea C. P., Houck J., Donahue M., Baum S., Voit M., O’Connell R. W., Koekemoer A., 2001, *ApJ*, 562, L149
- Mittal R., Hudson D. S., Reiprich T. H., Clarke T., 2009, *A&A*, 501, 835
- Nulsen P., Jones C., Forman W., Churazov E., McNamara B., David L., Murray S., 2009, in Heinz S., Wilcots E., eds, *American Institute of Physics Conference Series Vol. 1201 of American Institute of Physics Conference Series, Radio Mode Outbursts in Giant Elliptical Galaxies*. pp 198–201
- Nulsen P. E. J., David L. P., McNamara B. R., Jones C., Forman W. R., Wise M., 2002, *ApJ*, 568, 163
- Nulsen P. E. J., Johnstone R. M., Fabian A. C., 1987, *Proceedings of the Astronomical Society of Australia*, 7, 132
- Nulsen P. E. J., Jones C., Forman W. R., David L. P., McNamara B. R., Rafferty D. A., Bîrzan L., Wise M. W., 2007, in Böhringer H., Pratt G. W., Finoguenov A., Schuecker P., eds, *Heating versus Cooling in Galaxies and Clusters of Galaxies AGN Heating Through Cavities and Shocks*. p. 210
- Osmond J. P. F., Ponman T. J., 2004, *MNRAS*, 350, 1511
- O’Sullivan E., Giacintucci S., David L. P., Vrtilek J. M., Raychaudhury S., 2010, *MNRAS*, 407, 321
- O’Sullivan E., Vrtilek J. M., Harris D. E., Ponman T. J., 2007, *ApJ*, 658, 299
- Owen F. N., Ledlow M. J., 1997, *ApJS*, 108, 41
- Panagoulia E. K., Fabian A. C., Sanders J. S., 2013, *MNRAS*, 433, 3290
- Panagoulia E. K., Fabian A. C., Sanders J. S., 2014, *MNRAS*, 438, 2341
- Pandge M. B., Vagshette N. D., David L. P., Patil M. K., 2012, *MNRAS*, 421, 808
- Peres C. B., Fabian A. C., Edge A. C., Allen S. W., Johnstone R. M., White D. A., 1998, *MNRAS*, 298, 416
- Peterson J. R., Fabian A. C., 2006, *Phys. Rep.*, 427, 1
- Plana H., Boulesteix J., Amram P., Carignan C., Mendes de Oliveira C., 1998, *A&AS*, 128, 75
- Pratt G. W., Croston J. H., Arnaud M., Böhringer H., 2009, *A&A*, 498, 361
- Rafferty D. A., Bîrzan L., Nulsen P. E. J., McNamara B. R., Brandt W. N., Wise M. W., Röttgering H. J. A., 2013, *MNRAS*, 428, 58
- Rafferty D. A., McNamara B. R., Nulsen P. E. J., Wise M. W., 2006, *ApJ*, 652, 216
- Randall S. W., Forman W. R., Giacintucci S., Nulsen P. E. J., Sun M., Jones C., Churazov E., David L. P., Kraft R., Donahue M., Blanton E. L., Simionescu A., Werner N., 2011, *ApJ*, 726, 86
- Reiprich T. H., Böhringer H., 2002, *ApJ*, 567, 716
- Romanishin W., Hintzen P., 1988, *ApJ*, 324, L17
- Sanders J. S., Fabian A. C., 2002, *MNRAS*, 331, 273
- Sanders J. S., Fabian A. C., 2007, *MNRAS*, 381, 1381
- Sanders J. S., Fabian A. C., Allen S. W., Schmidt R. W., 2004, *MNRAS*, 349, 952

- Sanders J. S., Fabian A. C., Taylor G. B., 2009, MNRAS, 393, 71
- Soker N., 2003, MNRAS, 342, 463
- Trinchieri G., Breitschwerdt D., Pietsch W., Sulentic J., Wolter A., 2007, A&A, 463, 153
- Tucker W. H., Rosner R., 1983, ApJ, 267, 547
- Valluri M., Anupama G. C., 1996, AJ, 112, 1390
- Venturi T., Bardelli S., Zambelli G., Morganti R., Hunstead R. W., 2001, MNRAS, 324, 1131
- Voigt L. M., Fabian A. C., 2004, MNRAS, 347, 1130
- Voigt L. M., Schmidt R. W., Fabian A. C., Allen S. W., Johnstone R. M., 2002, MNRAS, 335, L7
- Voit G. M., Cavagnolo K. W., Donahue M., Rafferty D. A., McNamara B. R., Nulsen P. E. J., 2008, ApJ, 681, L5
- Werner N., Oonk J. B. R., Sun M., Nulsen P. E. J., Allen S. W., Canning R. E. A., Simionescu A., Hoffer A., Connor T., Donahue M., Edge A. C., Fabian A. C., von der Linden A., Reynolds C. S., Ruszkowski M., 2014, MNRAS, 439, 2291
- Wise M. W., McNamara B. R., Nulsen P. E. J., Houck J. C., David L. P., 2007, ApJ, 659, 1153

APPENDIX A: *CHANDRA* AND *XMM-NEWTON* IMAGES

In this section, we present the corresponding 0.5–7.0 keV exposure-corrected, background-subtracted and unsharp-masked *Chandra* images, and the 0.5–7.0 keV background flare-cleaned and unsharp-masked *XMM-Newton* images for the sources in our sample. Two different sources are shown in each row, with the two left-hand and the two right-hand columns of each row containing images from two different sources. Each set of two columns shows the exposure-corrected and background-subtracted *Chandra* image, or the cleaned *XMM-Newton* image in the left-hand column, while the right-hand column shows the unsharp-masked image. Each background-subtracted, exposure-corrected or cleaned image has been smoothed with a 2-pixel Gaussian. The bar in each *Chandra* image is 0.5 arcmin long, while the bars in the *XMM-Newton* images are 3 arcmin long. The arrows indicate “certain” or “possible” cavities. The majority of the unsharp-masked images are the result of the subtraction of an 8-pixel Gaussian smoothed image from a 2-pixel Gaussian smoothed image.

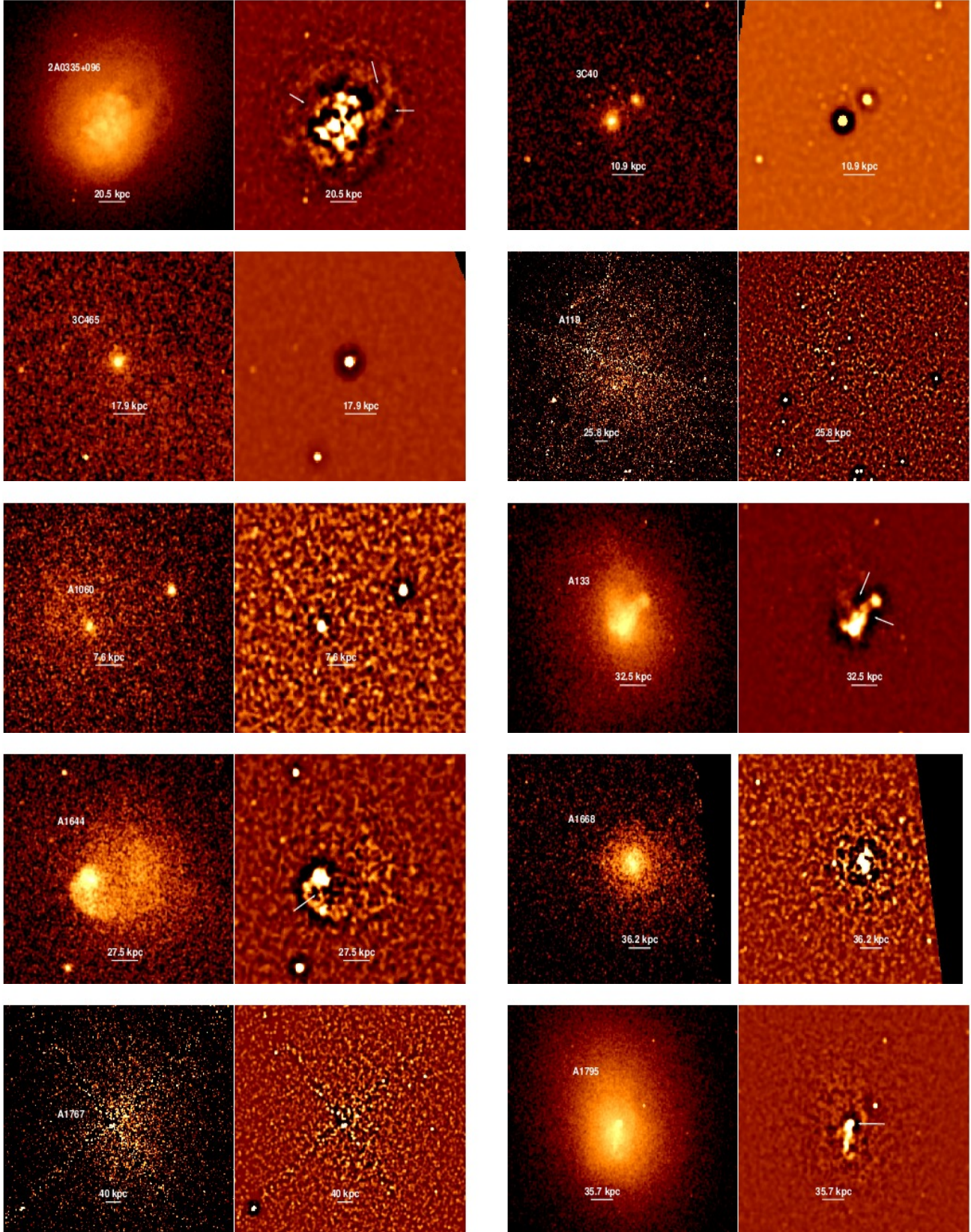


Figure A1. The bar is 0.5 arcmin long in all the *Chandra* images. All images have been created in the 0.5–7.0 keV band, and the background-subtracted, exposure-corrected images have been smoothed using a 2-pixel Gaussian. The left-hand panel for each set of two images shows the background-subtracted, exposure-corrected images, with the unsharp-masked image in the right-hand panel. The arrows indicate “possible” or “certain” cavities.

Figure A1 – *continued*

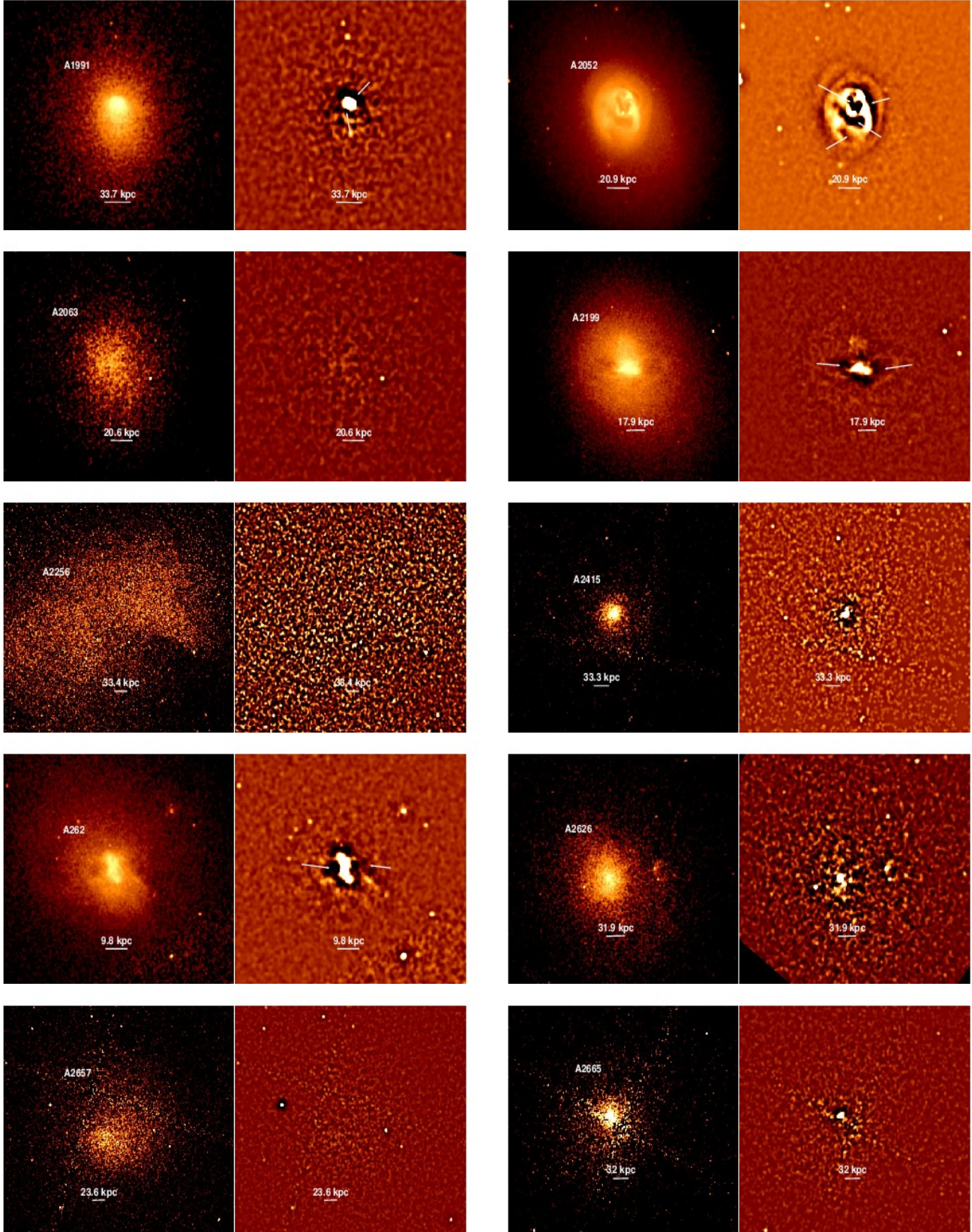


Figure A1 – *continued*

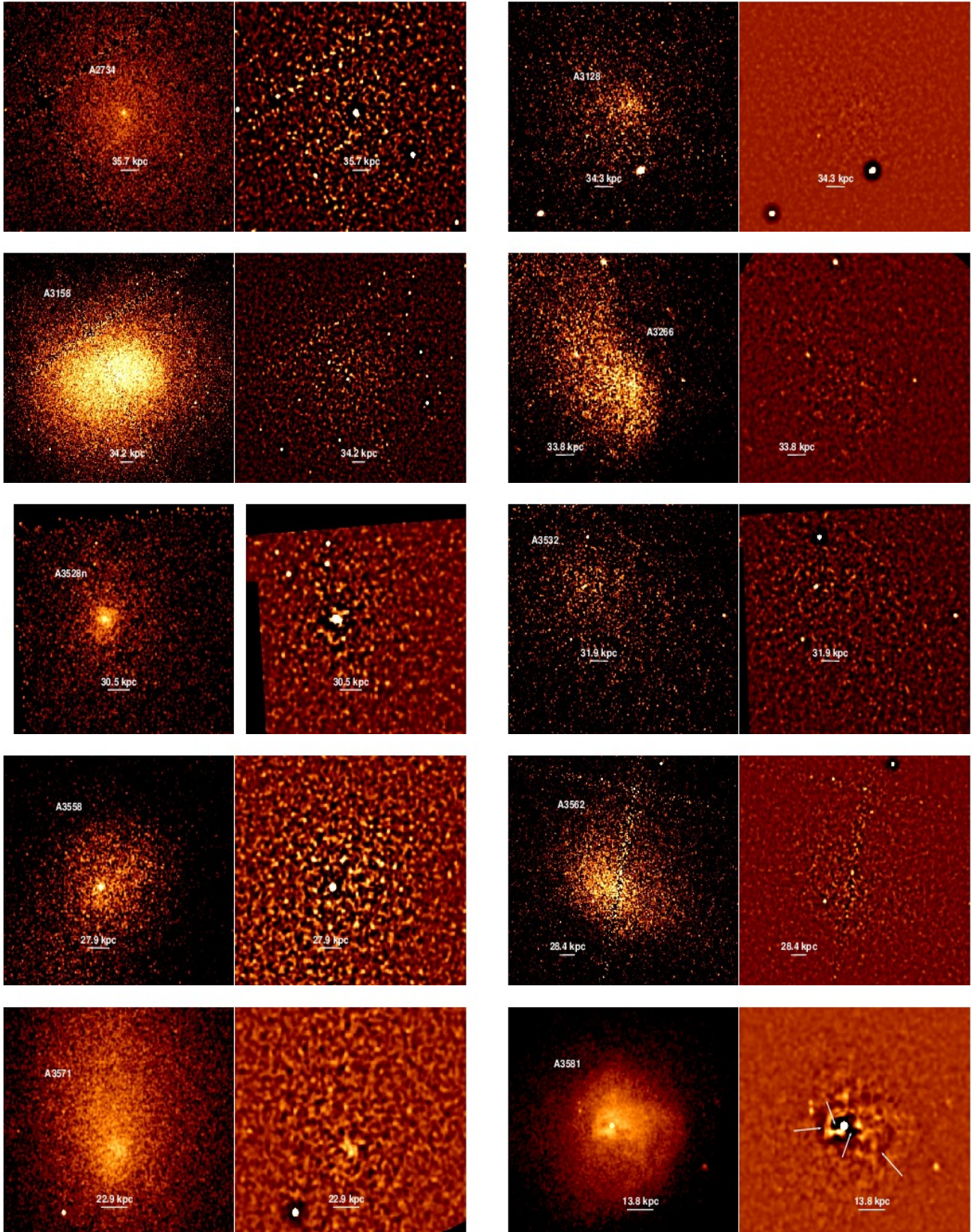


Figure A1 – *continued*

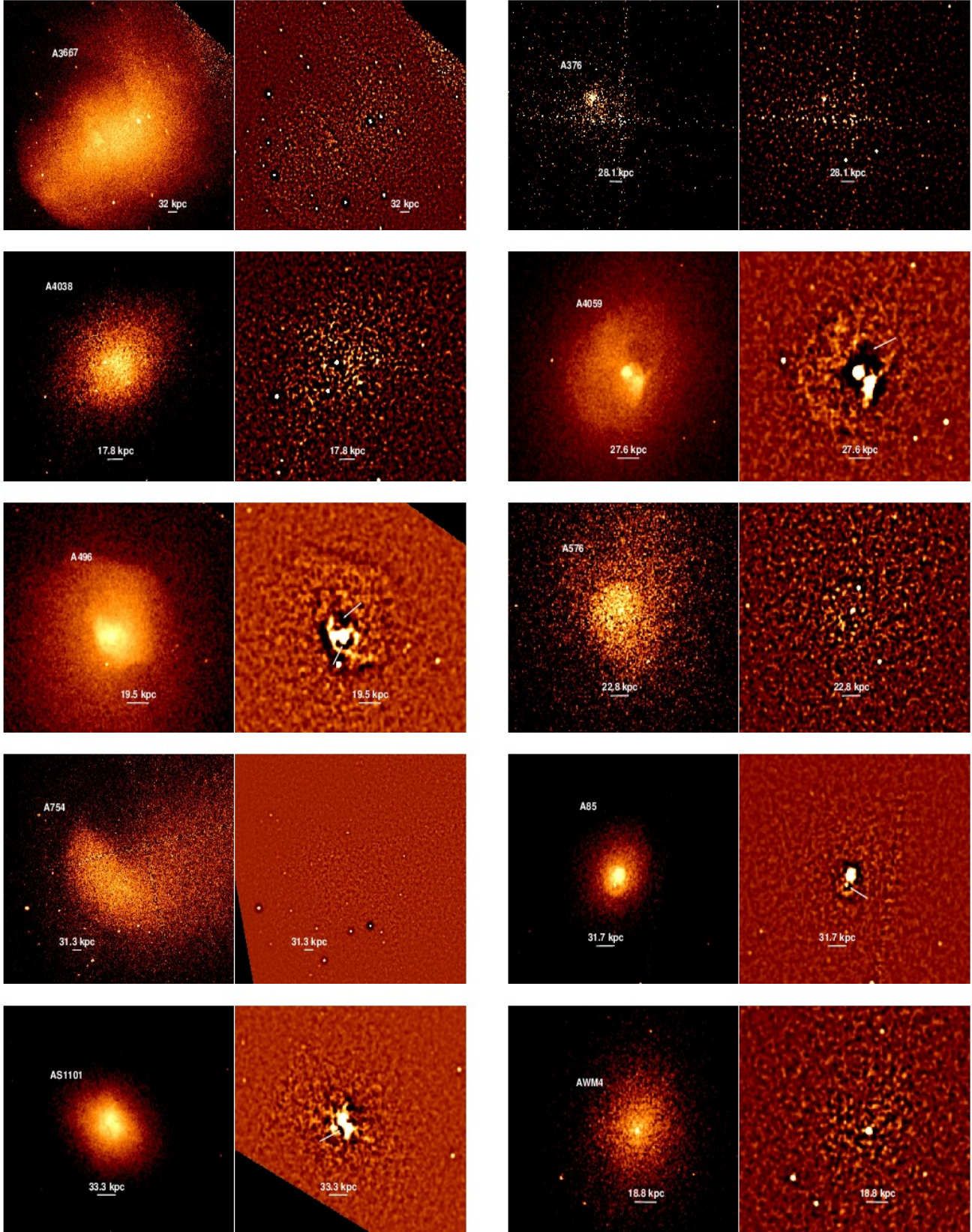


Figure A1 – *continued*

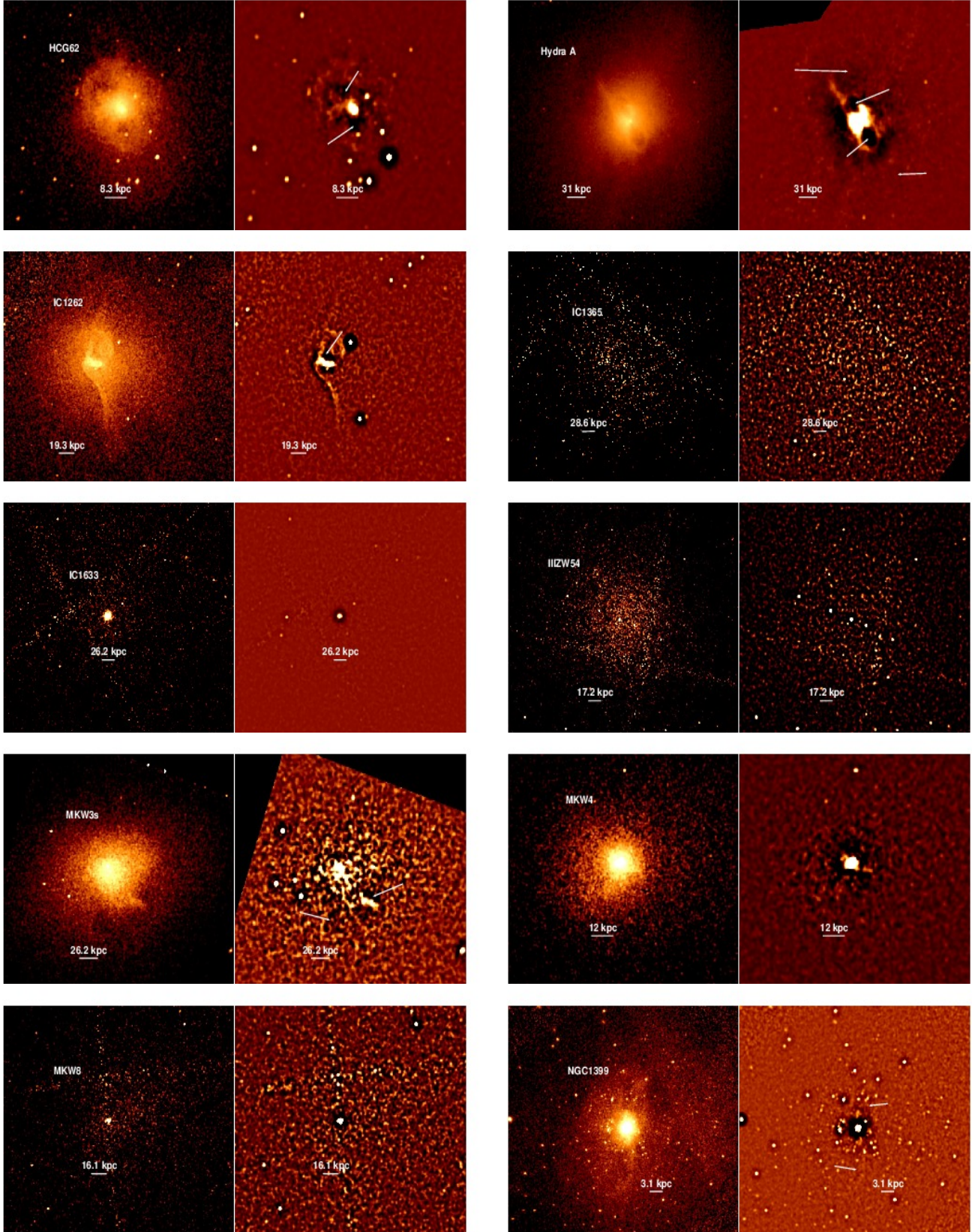


Figure A1 – *continued*

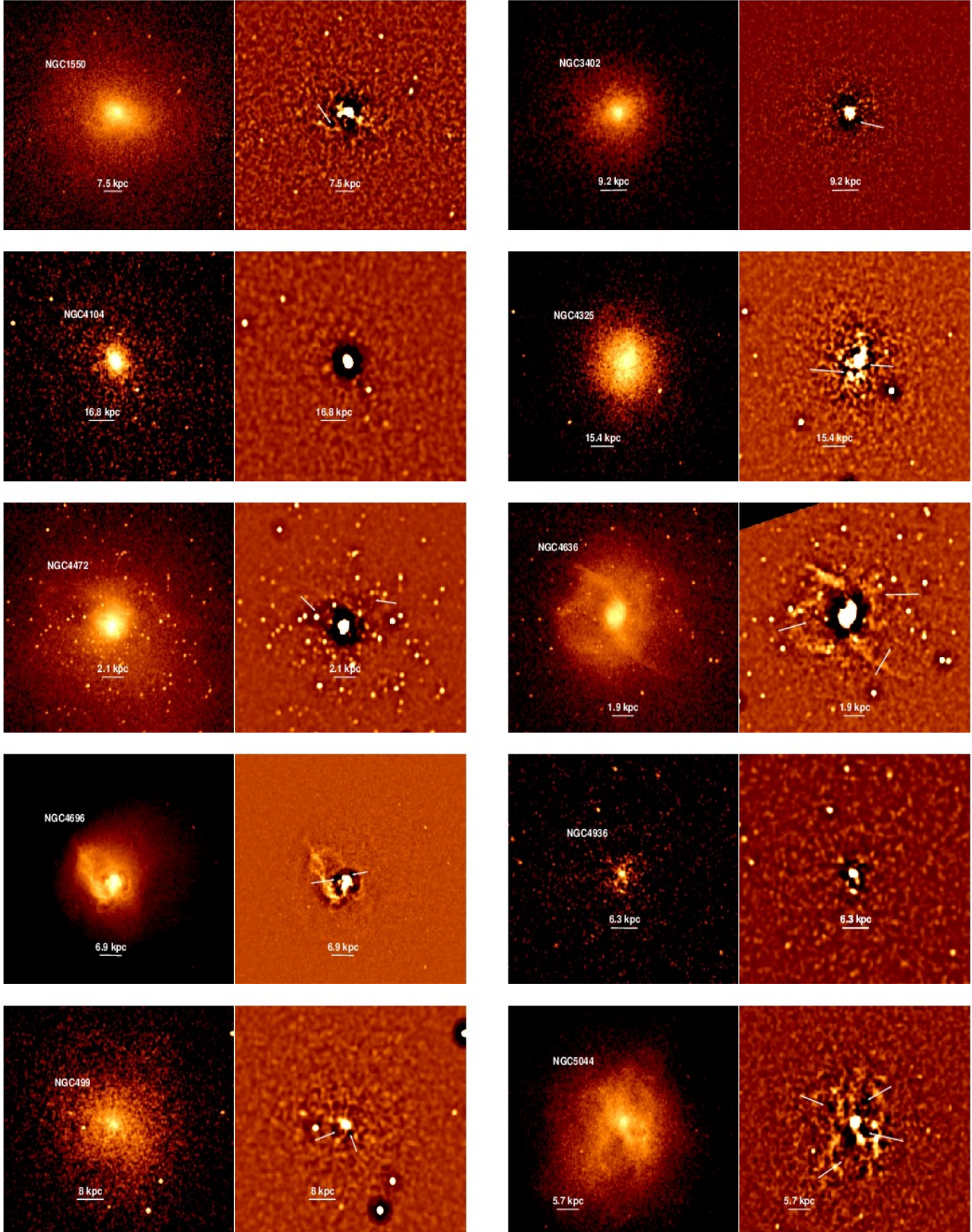


Figure A1 – *continued*

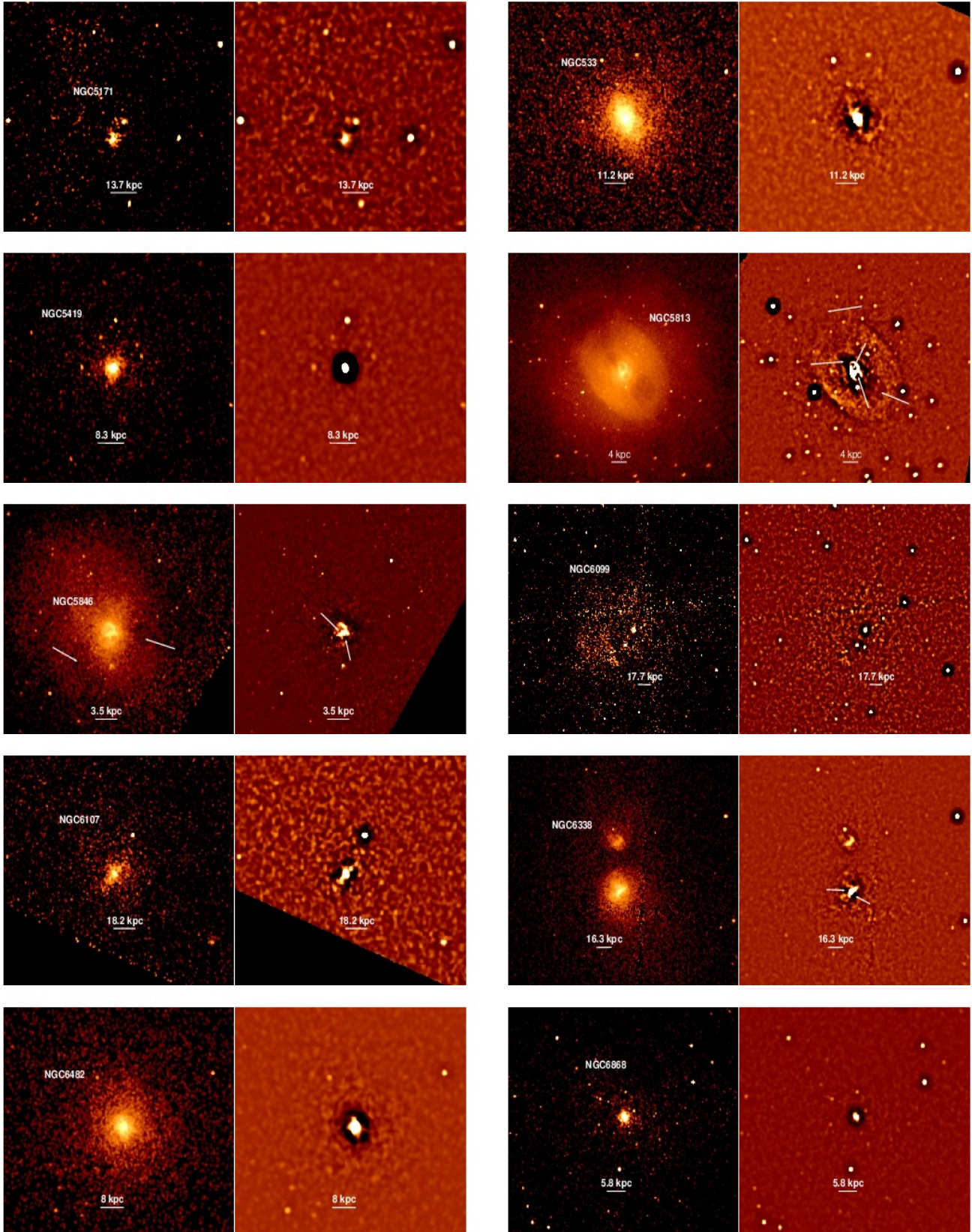
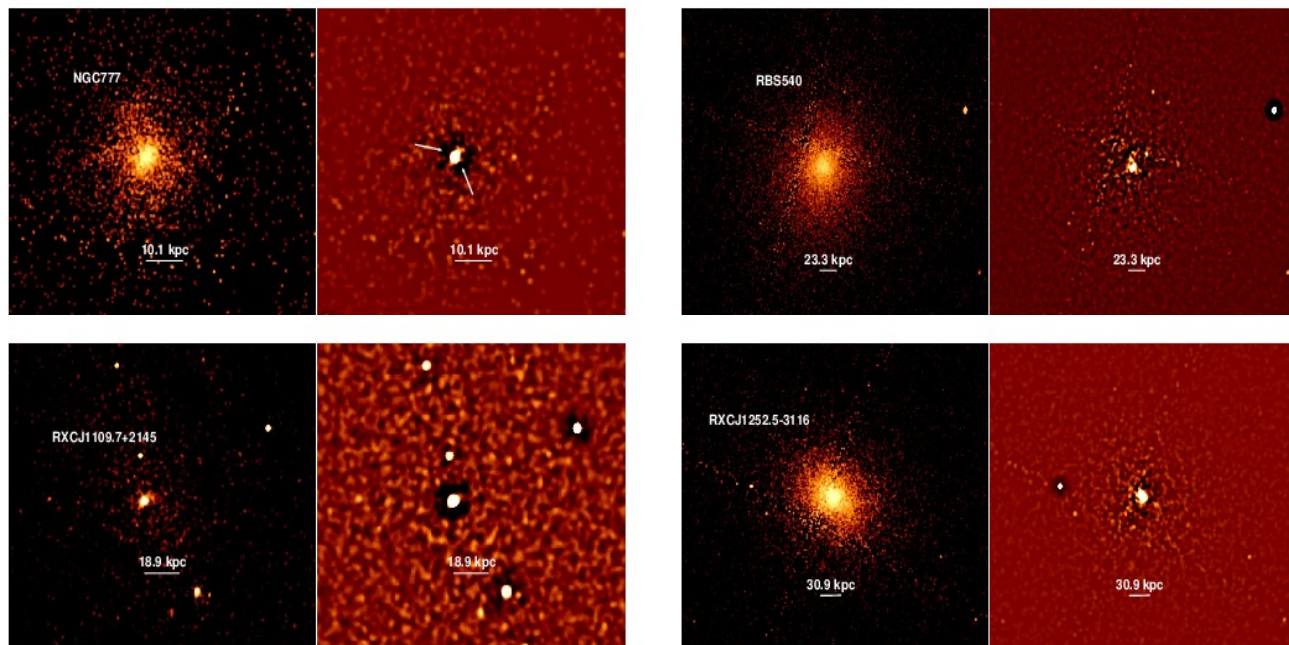


Figure A1 – *continued*



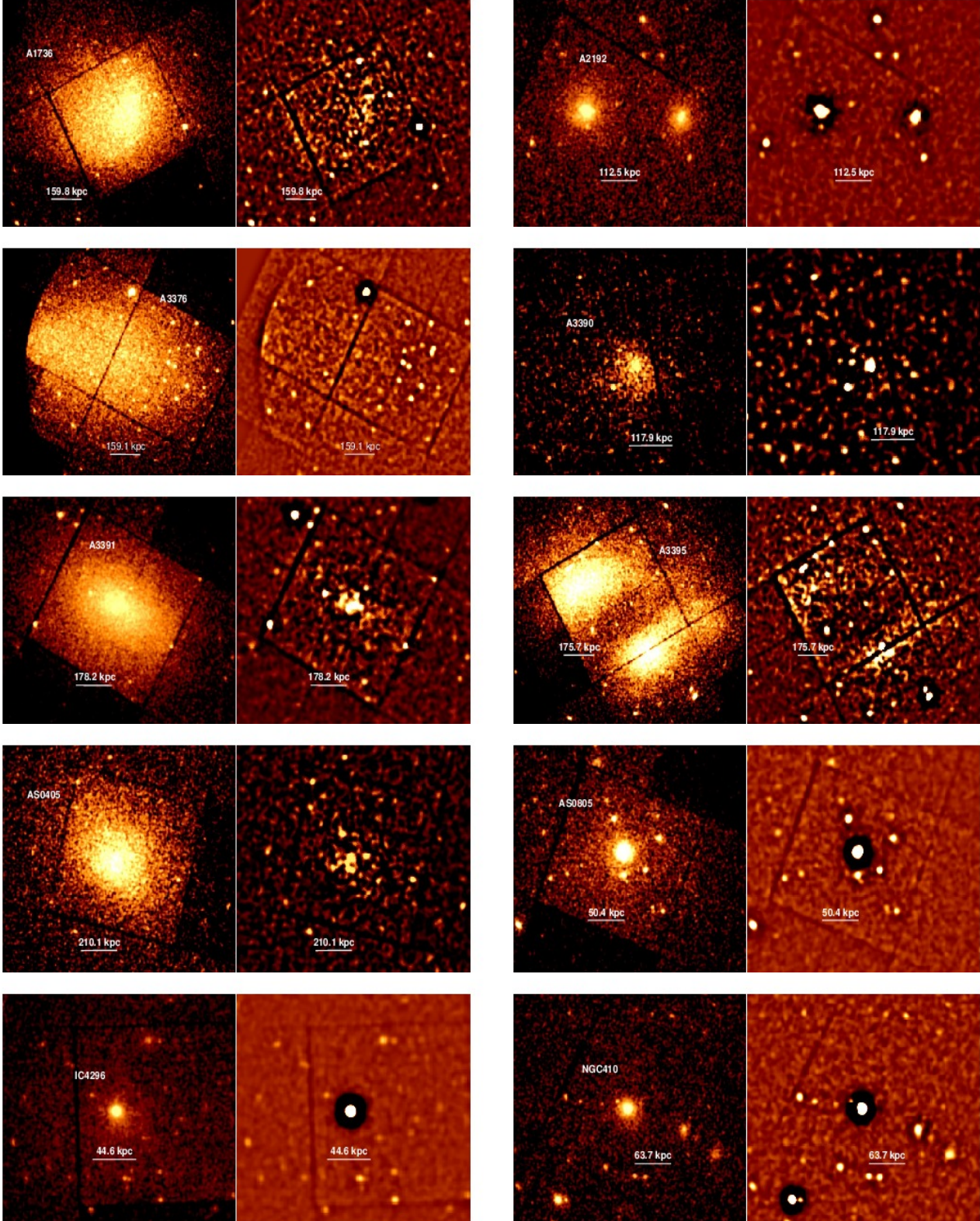


Figure A2. The bar is 3 arcmin long in all the images. All images were generated in the 0.5–7.0 keV energy band, and the original images have been smoothed using a 2-pixel Gaussian. The left-hand panel for each set of two images shows the cleaned images, with the unsharp-masked image in the right-hand panel. The arrows indicate “possible” or “certain” cavities.

Figure A2 – *continued*

